# AMG 193, a Clinical Stage MTA-Cooperative PRMT5 Inhibitor, Drives Antitumor Activity Preclinically and in Patients with MTAP-Deleted Cancers

Brian Belmontes[1], Katherine K. Slemmons[1], Chun Su[2], Siyuan Liu[1], Antonia N. Policheni[1], Jodi Moriguchi[1], Hong Tan[1], Fang Xie[2], Daniel Andrew Aiello[1], Yajing Yang[1], Raul Lazaro[1], Famke Aeffner[2], Matthew G. Rees[3], Melissa M. Ronan[3], Jennifer A. Roth[3], Mikkel Vestergaard[4], Sanne Cowland[4], Jan Andersson[4], Ian Sarvary[4], Qing Chen[1], Pooja Sharma[1], Patricia Lopez[1], Nuria Tamayo[1], Liping H. Pettus[1], Sudipa Ghimire-Rijal[1], Susmith Mukund[2], Jennifer R. Allen[1], Jason DeVoss[2], Angela Coxon[1], Jordi Rodon[5], François Ghiringhelli[6], Nicolas Penel[7], Hans Prenen[8], Sanne Glad[4], Chen-Hua Chuang[2], Kiana Keyvanjah[1], Danielle M. Townsley[1], John R. Butler[1], Matthew P. Bourbeau[1], Sean Caenepeel[1], and Paul E. Hughes[1]
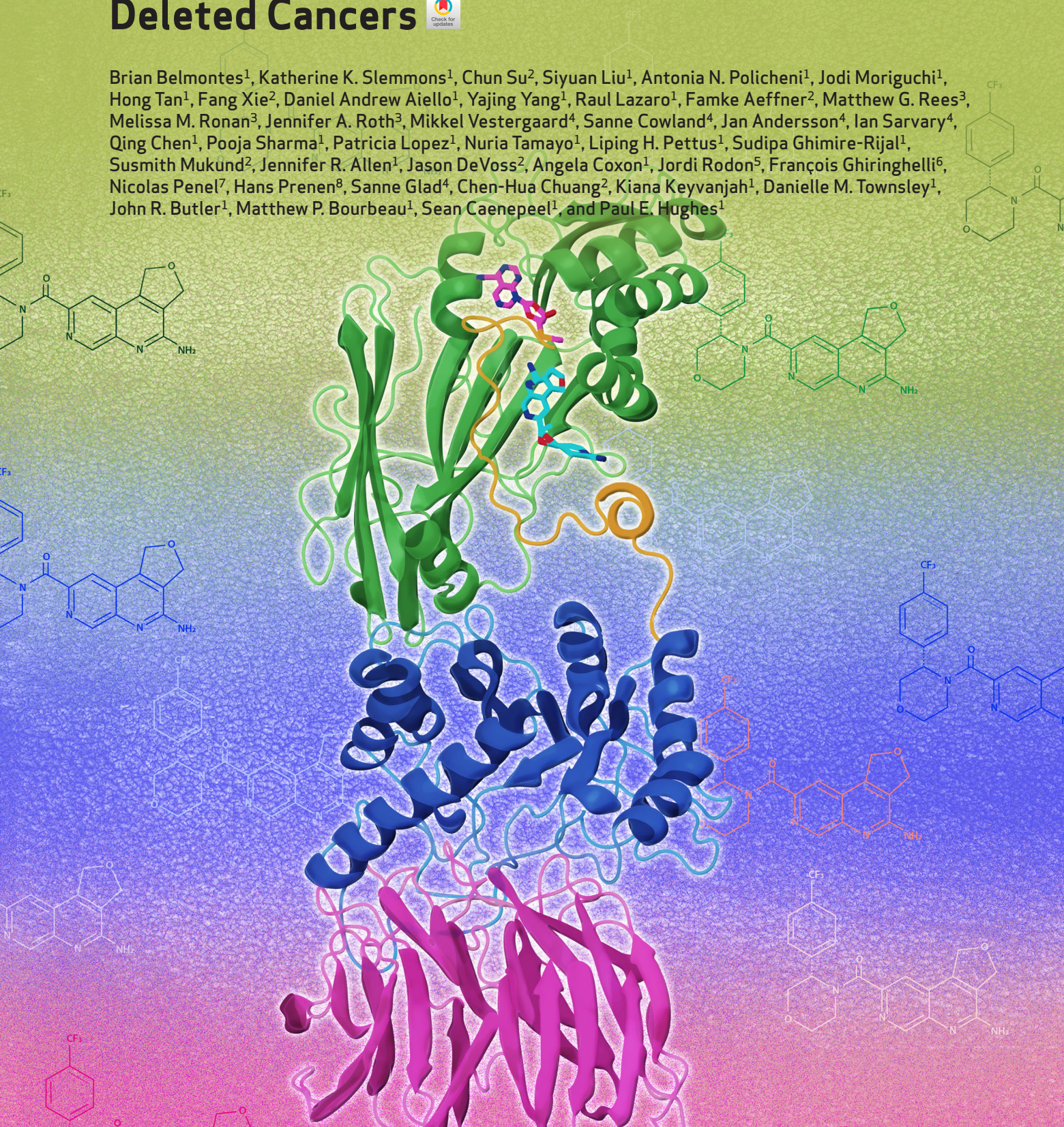
ABSTRACT   One of the most robust synthetic lethal interactions observed in multiple functional genomic screens has been the dependency on protein arginine methyltransferase 5 (PRMT5) in cancer cells with *MTAP* deletion. We report the discovery of the clinical stage MTA-cooperative PRMT5 inhibitor AMG 193, which preferentially binds PRMT5 in the presence of MTA and has potent biochemical and cellular activity in MTAP-deleted cells across multiple cancer lineages. *In vitro*, PRMT5 inhibition induces DNA damage, cell cycle arrest, and aberrant alternative mRNA splicing in MTAP-deleted cells. In human cell line and patient-derived xenograft models, AMG 193 induces robust antitumor activity and is well tolerated with no impact on normal hematopoietic cell lineages. AMG 193 synergizes with chemotherapies or the KRAS G12C inhibitor sotorasib *in vitro* and combination treatment *in vivo* substantially inhibits tumor growth. AMG 193 is demonstrating promising clinical activity, including confirmed partial responses in patients with MTAP-deleted solid tumors from an ongoing phase 1/2 study.

SIGNIFICANCE: AMG 193 preferentially inhibits the growth of MTAP-deleted tumor cells by inhibiting PRMT5 when in complex with MTA, thus sparing MTAP wild-type normal cells. AMG 193 shows promise as a targeted therapy in a clinically defined patient population.

INTRODUCTION

The development of therapies that selectively target proteins mutated in cancer has proven to be a highly effective and clinically validated therapeutic strategy for multiple cancer types (1). However, a substantial proportion of patients with cancer remain ineligible for targeted therapies because their tumors do not harbor genetic alterations that can be directly inhibited. One approach to overcome this limitation is to exploit synthetic lethality (2). A synthetic lethal interaction occurs between two genes when cancer cells can tolerate the perturbation of either gene alone but perturbation of both genes simultaneously results in a loss of viability. In one example of synthetic lethal cancer therapeutics, cancer cells that carry inactivation of "A" are specifically killed by the pharmacologic inhibition of "B," whereas normal cells that lack the genetic alteration in "A" are spared the toxic effect of the drug. Clinical validation of synthetic lethality has been achieved with the approval of multiple PARP inhibitors to treat *BRCA1* and *BRCA2*–mutated cancers (3–5). shRNA gene silencing and advances

in clustered regularly interspaced short palindromic repeats (CRISPR) gene editing technology have enabled the implementation of comprehensive functional genomic screens across large panels of genomically characterized cancer cell lines to identify genetic vulnerabilities and tractable drug targets that exploit synthetic lethality (6).

One of the most robust synthetic lethal interactions observed in multiple functional genomic screens has been the striking dependency on the protein arginine methyltransferase 5 (PRMT5) in cancer cells with homozygous codeletion of the tumor suppressor *CDKN2A* and the neighboring S-methyl-5-thioadenosine phosphorylase (*MTAP*) gene (7–10). Approximately 10% to 15% of human tumors have a genomic loss of this locus (referred to as MTAP-deleted for the resulting gene product) with enrichment in some tumors with a high clinical unmet need, such as pancreatic, lung, and glioblastoma (7). MTAP plays a central role in the adenine and methionine salvage pathways and homozygous deletion of *MTAP* results in the accumulation of the metabolite 5-methylthioadenosine (MTA; refs. 7–9). MTA is an inhibitory PRMT5 cofactor, competing with the methyl donor S-adenosylmethionine (SAM) for binding to PRMT5. Consequently, PRMT5 activity is partially inhibited in MTAP-deleted cancer cells, making these cells particularly vulnerable to further PRMT5 inhibition.

The cell-essential methyltransferase PRMT5 forms a complex with methylosome protein 50 (MEP50) to catalyze the symmetric dimethylation of arginine residues on a number of substrates, including transcription factors, histones, and members of the RNA spliceosome complex (11–13). Additionally, PRMT5 is upregulated in many cancers and has known roles in driving oncogenic growth (12, 13), making it an attractive therapeutic target. Multiple SAM-competitive or SAM-cooperative PRMT5 inhibitors have previously been described, and several of these molecules have advanced to the clinic (PF-06939999, GSK3326595, and JNJ-64619178; refs. 14–17).

[1]Amgen Research, Thousand Oaks, California. [2]Amgen Research, South San Francisco, California. [3]Broad Institute of MIT and Harvard, Cambridge, Massachusetts. [4]Amgen Research, Copenhagen, Denmark. [5]MD Anderson, Houston, Texas. [6]Centre Georges François Leclerc, Dijon, France. [7]Centre Oscar Lambret, Lille, France. [8]Universitair Ziekenhuis Antwerpen, Edegem, Belgium.

B. Belmontes and K.K. Slemmons contributed equally to this article.

Corresponding Author: Paul E. Hughes, Amgen Research, One Amgen Center Drive, Thousand Oaks, CA 91320–1799. E-mail: phughes@amgen.com

However, the activity of these molecules is not restricted to MTAP-deleted cells, and substantial on-mechanism hematologic toxicities were observed because of PRMT5 inhibition in non-transformed, MTAP wild-type (WT) cells (16, 17). We reasoned that a small molecule that specifically binds and inhibits PRMT5 in the presence of MTA would have the potential to selectively target MTAP-deleted cancer cells while sparing PRMT5 activity in MTAP WT cells.

Here, we report the discovery of the clinical stage MTA-cooperative PRMT5 inhibitor AMG 193. Using a DNA-encoded library (DEL), hits were identified with preferential binding to PRMT5 in the presence of MTA. Further optimization using structure-based drug design led to the orally bioavailable and potent AMG 193. In this study, we demonstrate the selectivity and activity of AMG 193 in a variety of MTAP-deleted tumor indications, including pancreatic, lung, and lymphoma. *In vitro* mechanism-of-action studies demonstrate that PRMT5 inhibition induces DNA damage, cell cycle arrest in G2/M, and an increase in alternative mRNA splicing in MTAP-deleted cells. In human cancer cell line and patient-derived xenograft (PDX) mouse models, AMG 193 induces robust antitumor activity at well-tolerated doses, with no observable effects on normal hematopoietic lineages. We also highlight the utility of AMG 193 in combination strategies with standard-of-care (SOC) chemotherapies or targeted agents. AMG 193 is currently being evaluated in individuals with advanced MTAP-deleted solid tumors (ClinicalTrials.gov; NCT05094336). The initial results of this first-in-human (FIH) study have demonstrated the preliminary safety, tolerability, and clinical proof of concept with confirmed target engagement and encouraging preliminary clinical activity.

RESULTS

The Discovery of AMG 193, a Potent MTA-Cooperative PRMT5 Inhibitor

To identify small molecules that preferentially bind to PRMT5 in the presence of MTA, we screened a DEL against PRMT5:MEP50 (6 µmol/L) in the presence of either MTA (60 µmol/L) or Sinefungin (60 µmol/L, a SAM substitute; refs. 18, 19). DELs are large collections of combinatorial compounds, in which each molecule is tagged with an identifying DNA barcode. The DEL was synthesized by a tagged-split-and-pool chemistry approach to generate 98.4 million trimeric members. HIS-tagged PRMT5:MEP50 was incubated with DEL and cofactor and subjected to two cycles of binding to an anti-HIS matrix followed by wash-off of unbound DEL molecules and eluting bound molecules using heat. Enriched DEL molecules were identified using next-generation sequencing of barcodes, and candidate hits were resynthesized off DNA and assayed for PRMT5 inhibition in the presence/absence of MTA. This screening campaign resulted in the identification of aminoquinoline compound 1 (Fig. 1A) as an initial hit that binds to PRMT5 in the presence of MTA, with an IC_{50} of 9.23 µmol/L for HCT116 MTAP-deleted cells and 3.6× selectivity over the corresponding isogenic HCT116 MTAP WT cells in viability assays. Installation of a C3-Me on the quinoline ring and replacement of the bis-substituted

benzyl amide in compound 1 with (*R*)-*N*-[1-(pyrimidin-2-yl)ethyl]-*N*-[(5-(trifluoromethyl)pyridin-2-yl)methyl] amide resulted in AM-9747 that demonstrated an improvement in potency (IC_{50} of 0.040 µmol/L in MTAP-deleted cells) and cooperativity (21×). AM-9747 displayed a pharmacokinetic (PK) profile [mouse intravenous clearance (2.3 L/hours/kg) and bioavailability (%F = 23)] suitable for *in vivo* proof-of-concept studies (Supplementary Table S1; ref. 20). Subsequent lead optimization using structure- and property-based drug design led us to the discovery of the tricyclic amide AMG 193, which was potent (IC_{50} of 0.107 µmol/L in MTAP-deleted cells), MTA-cooperative (40×), and orally bioavailable in preclinical species (Supplementary Table S1).

The X-ray cocrystal structure of AMG 193 in the active site of MTA-bound PRMT5: MEP50 was determined (Fig. 1B; Supplementary Table S2). The structure reveals that the amino-dihydrofuro-[1,7] naphthyridine motif in AMG 193 occupies the substrate-binding pocket of PRMT5 forming a strong polar interaction with the sidechain of Glu444, an H-bond with the backbone carbonyl of Glu435 and a tight van der Waals interaction between the methylene group of the dihydrofuran ring with the sulfur atom of MTA that also interacts with the NH_2 group of AMG 193. Additionally, the dihydrofuran ring is in a π–π stacking interaction with the sidechains of both Trp579 and Phe327, whereas the O-atom makes an H-bond with the amino side chain of Lys333. This side chain normally interacts with the carbonyl terminus of SAM, and the binding of AMG 193 causes Lys333 to move away from the SAM binding site. This series of contacts contributes to the selectivity and MTA cooperativity observed with AMG 193 (Fig. 1B). This structure illustrates the trimeric complex that is formed between AMG 193, MTA, and PRMT5; therefore, AMG 193 was considered an MTA-cooperative PRMT5 inhibitor.

Surface plasmon resonance (SPR) assays were developed in the presence of MTA and SAM to determine AMG 193 and PRMT5 binding affinity (K_D), kinetics [association (k_a) and dissociation (k_d) rates], *in vitro* half-life ($t_{1/2}$), and MTA cooperativity. Analysis of SPR direct binding revealed that AMG 193 forms a very stable complex with PRMT5 in the presence of MTA. The ternary complex has an extremely slow dissociation with a k_d of 1.0E−04 1/s ($t_{1/2} > 120$ minutes). In contrast, the SPR direct-binding assay revealed that AMG 193 bound to the PRMT5-SAM complex (Fig. 1C) in a less stable manner with a much faster dissociation rate, shorter half-life ($t_{1/2} < 30$ minutes), and a weaker binding affinity ($K_D = 0.23$ nmol/L). This reduced affinity led to a lower percentage binding occupancy of AMG 193 in the presence of SAM compared with MTA (~25% *vs.* 94%). The slow dissociation rate of AMG 193 with the PRMT5-MTA complex prevented the calculation of an accurate binding dissociation rate constant from the direct-binding assay. We therefore developed an SPR chaser assay (21, 22) using a chaser molecule (compound 2, an AMG 193 competitor; Supplementary Figs. S1A–S1C and S2A). The chaser molecule is an MTA-independent PRMT5 binder with an affinity of 6 nmol/L (±MTA) and a short half-life ($t_{1/2} < 10$ minutes; Supplementary Fig. S1A–S1C). The SPR chaser assay (Supplementary Fig. S2B; Fig. 1D) confirmed that AMG 193 binds to the PRMT5-MTA complex with an extremely high affinity (3.9 pmol/L), producing a stable complex with very
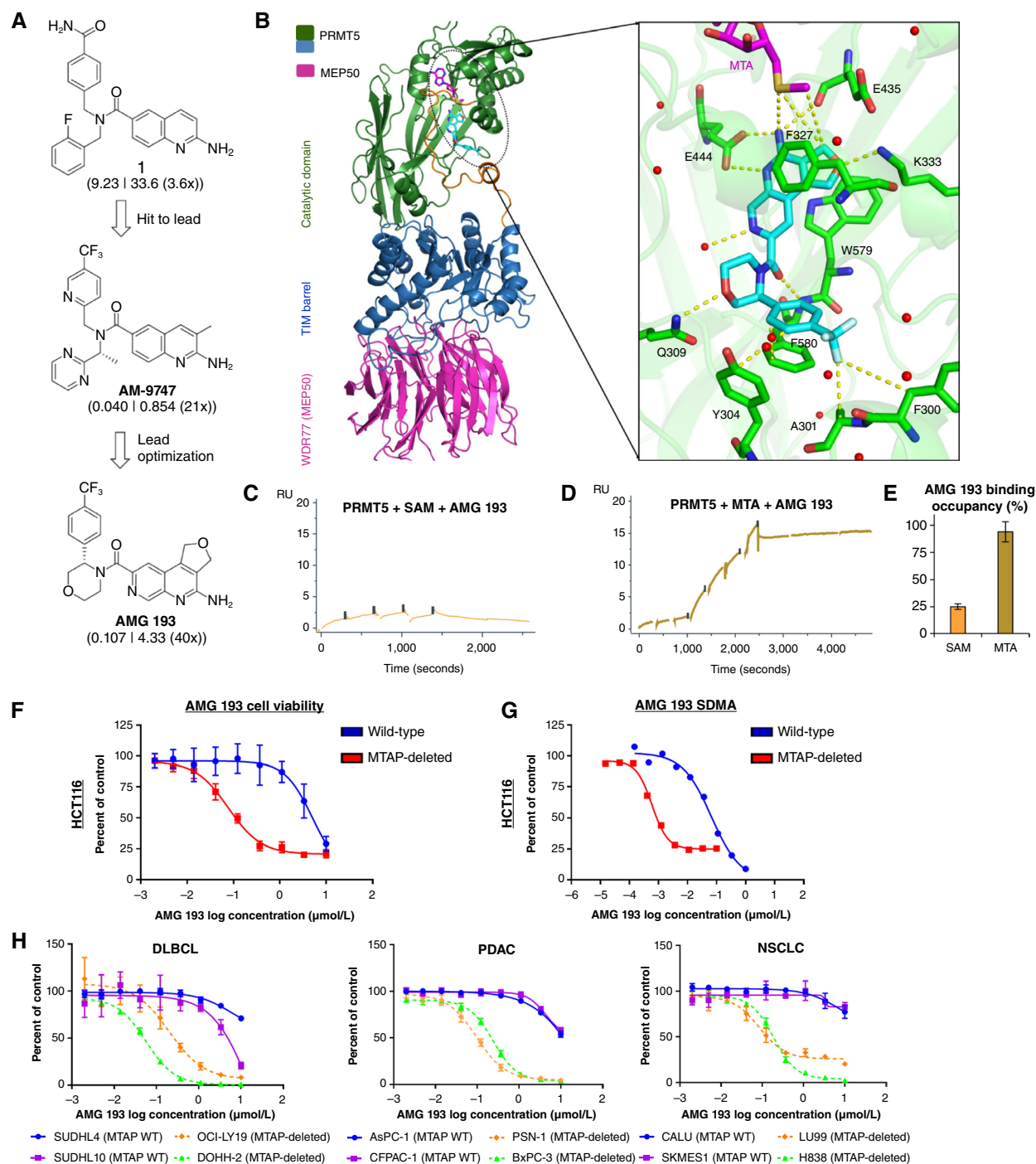
Figure 1. AMG 193 preferentially inhibits viability and SDMA signaling in MTAP-deleted tumor cells. **A,** Schematic demonstrates hit to lead to AMG 193 discovery. Cellular potency [HCT116 MTAP-deleted | WT viability IC$_{50}$ (μmol/L)] and MTA cooperativity of compound 1, AM-9747, and AMG 193 are shown beneath the structures. **B,** Cocrystal structure of AMG 193 in complex with MTA-bound PRMT5:MEP50 at 2.55 Å resolution (PDB: 9C10). The inset shows the ligand binding site. Cyan, AMG 193; salmon, MTA; red, water; green, PRMT5. Key contacts are shown with yellow dashed lines. The figures were generated with the PyMOL Molecular Graphics System, Version 1.7.0.1 Schrödinger, LLC. **C** and **D,** SPR sensorgrams of AMG 193 direct binding with PRMT5 in the presence of 20 μmol/L SAM and 20 μmol/L MTA. Histogram analysis depicts the percentage average binding surface occupancy of AMG 193 with or without MTA. **E,** Histogram analysis depicts the averaged percentage of PRMT5 surface occupancy by AMG 193 in the presence of SAM or MTA. **F,** HCT116 WT and MTAP-deleted cells were treated with AMG 193 or DMSO-only control for 6 days. Viability was measured by CTG and cooperativity was determined as follows: Cooperativity = WT IC$_{50}$/MTAP-deleted IC$_{50}$ (mean ± SD, $n = 3$). **G,** HCT116 WT and MTAP-deleted global SDMA levels were assessed by an in cell imaging assay after 3 days of treatment with AMG 193. Each cell line was normalized to its own DMSO-only control. **H,** Representative dose-response curves of DLBCL, PDAC, and NSCLC WT and MTAP-deleted cell lines treated with AMG 193 for 6 days, and cell viability was measured by CTG. CTG, CellTiter-Glo; MTA, methylthioadenosine; MTAP, methylthioadenosine phosphorylase; NSCLC, non–small cell lung cancer; PRMT5, protein arginine methyltransferase 5; RU, response units; SDMA, symmetric dimethylarginine; SPR, surface plasmon resonance; WT, wild-type.

slow dissociation rate ($k_d = 7.78E{-}06$ 1/s and $t_{1/2}$ ~25 hours) and a high binding surface occupancy of ~94% [of normalized % of the maximum number of iterations (R_{max}; Fig. 1D and E)]. AMG 193 cooperativity was calculated by comparing the SPR affinity of AMG 193 with PRMT5-MTA versus the PRMT5-SAM complex. Overall, in the presence of MTA, AMG 193 binds to PRMT5 approximately 60-fold more potently with approximately 70% higher binding surface occupancy and in a highly stable complex with extremely slow dissociation rates. SPR analysis further corroborates the observation that AMG 193 is an MTA-cooperative binder and inhibitor of PRMT5.

MTAP-Deleted Cancer Cells Exhibit Increased Sensitivity to MTA-Cooperative PRMT5 Inhibitors

To understand the effects of the MTA-cooperative PRMT5 inhibitors on cancer cell viability and signaling, we utilized the isogenic MTAP WT and MTAP-deleted HCT116 cells. MTAP protein loss was confirmed by immunoblot (Supplementary Fig. S3A and S3B). First, to assess the effects on cell viability, the HCT116 isogenic pair was treated with AMG 193 or the tool compound AM-9747 for 6 days (Fig. 1F and G; Supplementary Fig. S4A and S4B). A dose-dependent decrease in cell viability was observed in both the WT and MTAP-deleted cells. However, the MTAP-deleted cells were more sensitive to MTA-cooperative PRMT5 inhibitors with a 46-fold lower IC_{50} (Fig. 1F). Global symmetric dimethylarginine (SDMA) levels also decreased in a dose-dependent manner, with the MTAP cells exhibiting a 90-fold lower IC_{50} value (Fig. 1G). Immunoblot analysis also confirmed SDMA inhibition after AM-9747 treatment in the HCT116 isogenic pair (Supplementary Fig. S3B). These data demonstrate that the MTA-cooperative PRMT5 inhibitors AMG 193 and AM-9747 can preferentially inhibit SDMA levels and cell viability in MTAP-deleted cells. The tool compound AM-9747 was used in a variety of applications to uncover the biology of MTA-cooperative PRMT5 inhibitors while AMG 193 was under development. In preclinical assessments, AM-9747 and AMG 193 have similar *in vitro* and *in vivo* biology and can be used interchangeably (Supplementary Table S3). AMG 193 progressed clinically due to improved *in vivo* potency and PK properties (Supplementary Table S1).

Next, we tested the MTA-cooperative PRMT5 inhibitor AM-9747 or the noncooperative PRMT5 inhibitor LLY-283 (23) in a panel of endogenous MTAP WT and MTAP-deleted cancer cells. Although MTAP status did not track closely with sensitivity to the noncooperative inhibitor LLY-283, MTAP-deleted cells had preferential sensitivity to AM-9747, with IC_{50} values of <100 nmol/L (Supplementary Fig. S4C). Representative dose-response curves demonstrated a clear separation between WT and MTAP-deleted lines across tumor types with high occurrences of MTAP deletion, including diffuse large B-cell lymphoma (DLBCL), pancreatic ductal adenocarcinoma (PDAC), and non–small cell lung cancer (NSCLC; Fig. 1H; Supplementary Fig. S4D). For most WT cell lines, accurate IC_{50} values could not be calculated because the curves did not reach 50% of control. Of note, MTAP-deleted DLBCL lines were exquisitely sensitive to PRMT5 inhibition, with 10-fold lower IC_{50} values than other indications [Fig. 1H; Supplementary Fig. S4D (left)]. Target inhibition and MTAP

status were confirmed across the cell line panel by immunoblots for SDMA and MTAP, respectively (Supplementary Fig. S5A–S5C). We conclude that the MTA-cooperative PRMT5 inhibitors AM-9747 and AMG 193 drive the preferential killing of MTAP-deleted cells.

MTA-Cooperative PRMT5 Inhibition Induces Alternative Splicing Defects, Cell Cycle Arrest, and DNA Damage Response in MTAP-Deleted Cells

To investigate the mechanism of action (MOA) of the MTA-cooperative PRMT5 inhibitors, we assessed the global gene expression alterations induced by PRMT5 inhibition using RNA sequencing (RNA-seq). RNA-seq analysis of three MTAP-deleted pancreatic cancer cell lines treated with AM-9747 revealed substantial gene expression changes after PRMT5 inhibition (Supplementary Fig. S5D). Gene set enrichment analysis showed that the gene expression changes clustered in pathways related to cell cycle and RNA processing (Supplementary Fig. S5E). In line with previous studies (11, 24, 25), PRMT5 inhibition resulted in a global change in alternative splicing events, with a strong increase in retained introns (Supplementary Fig. S5F). Most of these alternative splicing events occurred in genes involved in RNA splicing and mRNA processing as shown by pathway analysis (Supplementary Fig. S5G), consistent with the role of PRMT5 in regulating the spliceosome. Together, these data suggest that mechanistically MTA-cooperative PRMT5 inhibitors impact cell growth through changes in cell cycle gene expression and an increase in alternative mRNA splicing.

To investigate the consequences of PRMT5 inhibition on the cell cycle, paired isogenic HCT116 cell lines were treated with a panel of PRMT5 inhibitors and processed for cell cycle analysis by flow cytometry. AM-9747 treatment showed a selective decrease in S-phase and an increase in the G_2/M cell population in the MTAP-deleted cells relative to WT cells (Fig. 2A). In contrast, treatment with the noncooperative PRMT5 inhibitor EPZ015666 (EPZ) resulted in similar profiles in both WT and MTAP-deleted cells. In a panel of DLBCL WT and MTAP-deleted cells, AM-9747 treatment selectively induced cell death as measured by the marked increase in the sub-G_1 population only in the MTAP-deleted cells (Fig. 2B). A panel of endogenous MTAP-deleted solid tumor cell lines treated with AM-9747 showed comparable cell cycle effects as the HCT116 MTAP-deleted isogenic cells (Fig. 2C). In line with these findings, AM-9747 and AMG 193 both exhibited similar cell cycle effects in the MTAP-deleted NSCLC cell line H838 (Supplementary Fig. S5H).

PRMT5 has established roles in regulating the DNA damage response (DDR) in cancer cells, and noncooperative PRMT5 inhibitors have been shown to drive increased DNA damage in tumor cells (24). To determine if our MTA-cooperative PRMT5 inhibitors impacted the DDR, multiple DNA damage endpoints were assessed after AM-9747 treatment. First, a single-cell gel electrophoresis assay (comet assay) was performed in DOHH-2 DLBCL cells and BxPC-3 PDAC cells after AM-9747 treatment. A substantial increase in comet tail length was observed after AM-9747 treatment relative to DMSO control, consistent with increased DNA strand breaks (Fig. 2D and E). Second, high-content imaging
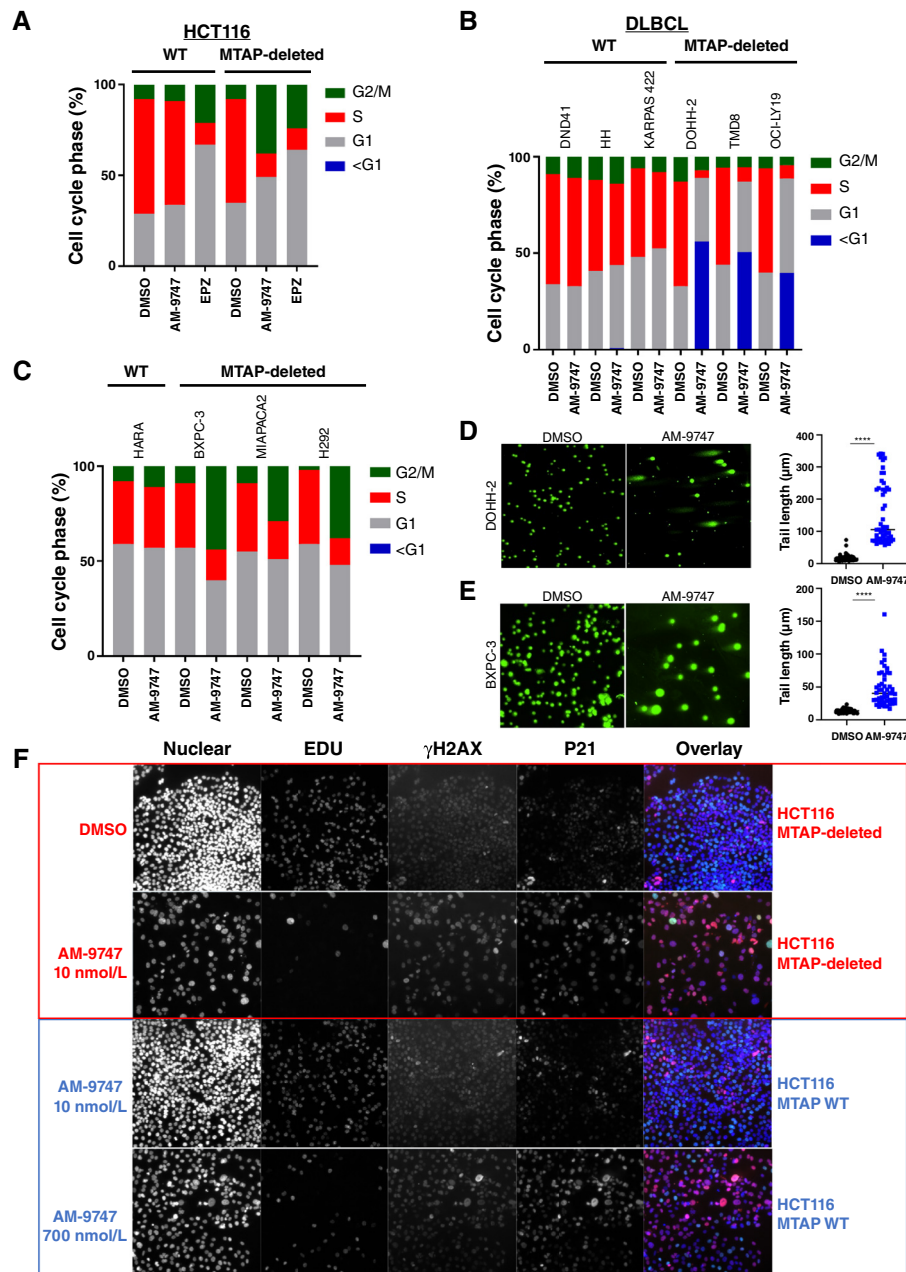
Figure 2. AM-9747 treatment results in cell cycle arrest and increased DNA damage. **A,** Cell cycle analysis in HCT116 WT and MTAP-deleted cells treated with 200 nmol/L AM-9747 or 10 µmol/L EPZ for 6 days. **B,** Cell cycle analysis in WT or MTAP-deleted DLBCL cells or (**C**) solid tumor cell lines after 6 days of treatment with 100 nmol/L AM-9747. Comet assays to detect DNA damage in DOHH-2 DLBCL cells (**D**) or BxPC-3 pancreatic cells after treatment with 100 nmol/L AM-9747 (**E**). Comet tail length is quantified in the right hand of **D** and **E**. **F,** Representative high-content images of HCT116 MTAP-deleted cells (top) and HCT116 WT cells (bottom) treated with a dose titration of AM-9747 for 6 days. Cells were pulsed with EDU and stained with relevant antibodies before image acquisition. EPZ, EPZ015666; MTAP, methylthioadenosine phosphorylase; WT, wild-type.

analysis was performed to detect DNA synthesis [5-ethynyl-2′-deoxyuridine (EDU) incorporation], DNA damage markers (γH2AX, p21), and cell arrest (p21) markers in the HCT116 isogenic pair. PRMT5 inhibition by AM-9747 at low concentrations led to a decrease in EDU incorporation and an increase in γH2AX and p21 signals in the HCT116 MTAP-deleted cells (Fig. 2F). However, a 70-fold higher dose of AM-9747 was required to exhibit comparable levels of γH2AX and p21 signal in the HCT116 WT cells [(Fig. 2F (bottom)]. A similar decrease in

EDU and an increase in γH2AX and p21 signals were observed in the endogenous MTAP-deleted pancreatic line BxPC-3 after AM-9747 treatment (Supplementary Fig. S6A). Additionally, PRMT5 inhibition increased cellular senescence as observed by elevated β-galactosidase staining after AM-9747 treatment (Supplementary Fig. S6B). Taken together, these data show that selective PRMT5 inhibition in MTAP-deleted cells results in splicing defects and increased levels of DNA damage that drive cell death or growth arrest.

Comprehensive Cell Line Profiling with AMG 193 Confirms Sensitivity Is Correlated with MTAP Loss

To further assess the sensitivity and cooperativity of the MTA-cooperative PRMT5 inhibitor AMG 193, a large unbiased screen consisting of more than 850 cancer cell lines across multiple cancer indications was conducted using the Profiling Relative Inhibition Simultaneously in Mixtures (PRISM) platform (26, 27). Barcoded cancer cell lines were treated with an eight-point dose–response of AMG 193 for 5 days, and relative barcode abundance was used to generate cell line sensitivity profiles from the AUC values. The sensitivity profile for AMG 193 revealed a focal AMG 193 sensitivity in a subset of cell lines (Fig. 3A; Supplementary Table S4). AUCs varied across tumor lineages, with lower AUCs observed in some lineages like biliary tract and esophageal (Fig. 3B). Overall, the AMG 193 AUCs were substantially lower in MTAP-deleted cells compared with WT, and this relationship was maintained across specific lineages, including pancreatic, lung, and lymphoma (Fig. 3C). The available Cancer Dependency Map (DepMap) databases were used to correlate AMG 193 AUCs with copy number, RNA expression levels, and viability after whole genome RNAi knockdown or CRISPR knockout (Fig. 3D and E). The top genetic dependency from the RNAi knockdown dataset that correlated with sensitivity to AMG 193 was PRMT5, demonstrating that PRMT5-dependent lines show enhanced sensitivity to MTA-cooperative PRMT5 inhibitors [Fig. 3D (left)]. PRMT5 and its binding partner WDR77 were the top two associations in the CRISPR knockout dataset [Fig. 3D (right)]. Importantly, these data confirm the target specificity of AMG 193. Furthermore, the top genomic feature in terms of copy number and RNA expression was *MTAP*, further demonstrating the selectivity of this compound for MTAP-deleted tumor cells (Fig. 3E). As expected, *CDKN2A* and *CDKN2B* were the next top correlations for copy number and RNA expression because these genes are typically co-deleted with *MTAP*. In total, the PRISM screen confirmed AMG 193 sensitivity is correlated with *MTAP* and *CDKN2A* loss, as well as PRMT5 dependency across a large panel of cancer cell lines.

To follow up on the observation that PRMT5 inhibition induces alternative mRNA splicing, we hypothesized that cell lines with high rates of alternative splicing at baseline are more sensitive to PRMT5 inhibition. This aligns with prior observations that cancer cells with splice factor mutations are more sensitive to the first-generation noncooperative PRMT5 inhibitors due to the induction of aberrant splicing (11). To test this hypothesis, we analyzed the Cancer Cell Line Encyclopedia RNA-seq dataset (28) for alternative splicing events in the 129 MTAP-deleted cell lines [Fig. 3F (left); Supplementary Table S5]. We then determined the 371 events that are substantially associated with AMG 193 sensitivity using the $\log_2$AUC values from the PRISM screen (Supplementary Tables S4 and S6). These AMG 193-associated AS events are enriched in intron retention events, mostly with known annotated junctions [Fig. 3F (right)]. Known annotated junctions refer to junctions in which both isoforms involved in the event have corresponding transcripts identified in the reference gene model. Upon correlation with sensitivity to AMG 193 ($\log_2$AUC values), the intron retention rate is globally negatively associated with cell viability, suggesting that MTAP-deleted tumor cells with higher rates of intron retention are more sensitive to MTA-cooperative PRMT5 inhibitors (Fig. 3G). Further studies will be needed to understand if this association holds *in vivo* and in the clinical setting.

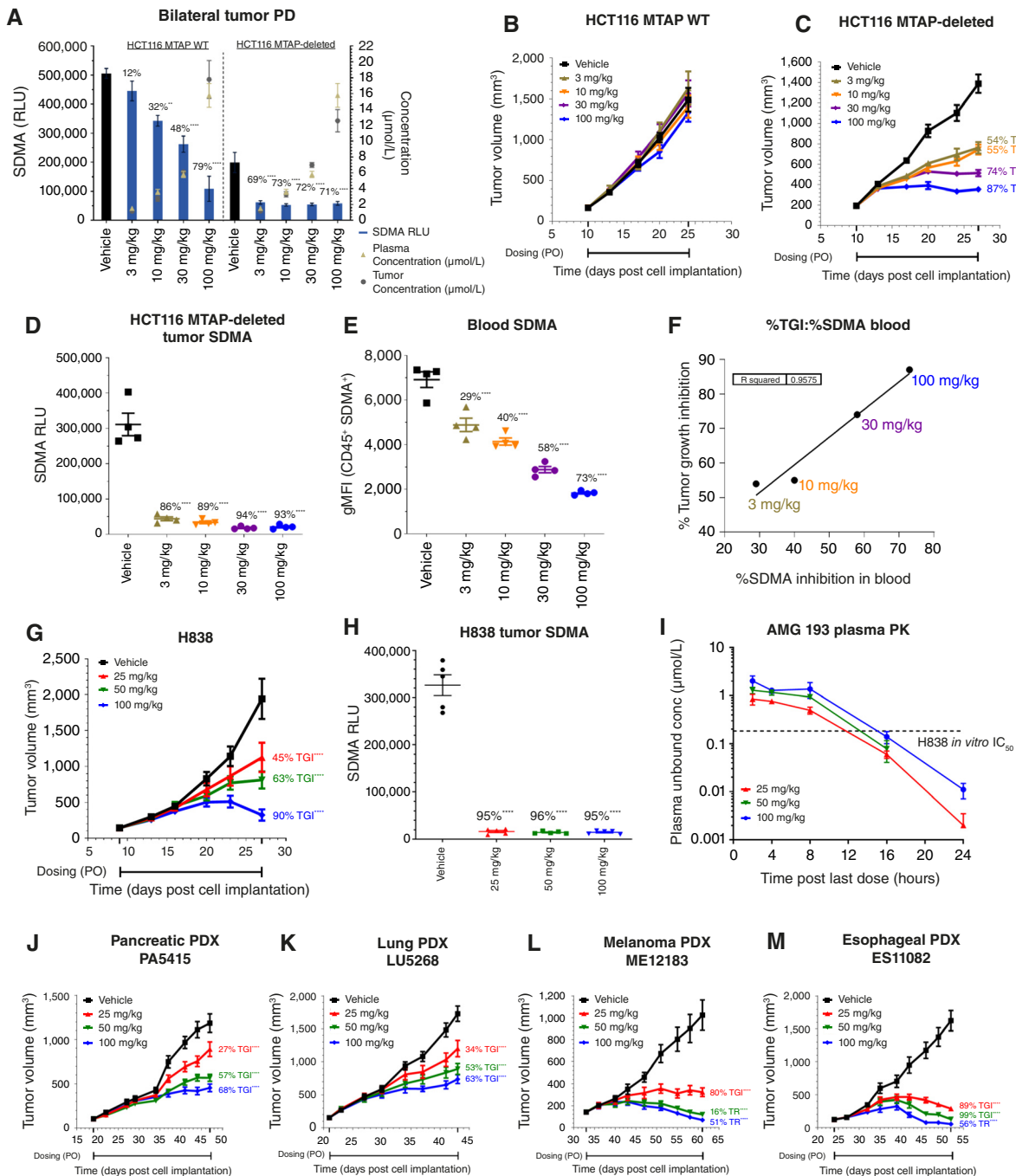## AMG 193 Inhibits the Growth of MTAP-Deleted Tumors *In Vivo*

To assess the potency and selectivity of AMG 193 *in vivo*, the HCT116 isogenic pair was used in cell line–derived xenograft (CDX) tumor models. First, AMG 193 was evaluated in a 4-day SDMA pharmacodynamic (PD) and PK study in mice implanted with MTAP-deleted cells on one flank and MTAP WT cells on the opposite flank. Mice were orally administered AMG 193 daily (QD) at four dose levels. AMG 193 treatment substantially inhibited SDMA signal, as measured by SDMA ELISA, in the MTAP-deleted tumors at all doses tested; however, only at the maximum dose of 100 mg/kg was >50% SDMA inhibition observed in MTAP WT tumors (Fig. 4A). We also assessed AMG 193 drug exposures in tumor and plasma in this study and demonstrated near-equivalent drug levels in tumor and plasma that were dose proportional (Fig. 4A). A follow-up time course study in HCT116 MTAP-deleted tumors revealed similar SDMA inhibition after 4 days of dosing, with maximal SDMA inhibition observed after 11 days of dosing and remaining consistently inhibited throughout the 21 days of AMG 193 treatment (Supplementary Fig. S7A). We next evaluated the antitumor effects of AMG 193 in the HCT116 MTAP WT and MTAP-deleted tumor xenografts. AMG 193 treatment did not inhibit the growth of HCT116 MTAP WT tumors at any of the doses evaluated (Fig. 4B). In contrast, AMG 193 demonstrated dose-dependent and statistically substantial tumor growth inhibition in MTAP-deleted xenografts (Fig. 4C). These data confirmed the selectivity and on-target activity of AMG 193 *in vivo*. Terminal tumors and blood were taken for SDMA analysis. SDMA was inhibited in a dose-dependent manner from 26% to 76% in HCT116 WT tumors (Supplementary Fig. S7B). In contrast, SDMA was almost completely inhibited, with 86% to 93% inhibition at the four dose levels tested in HCT116 MTAP-deleted tumors (Fig. 4D). These data demonstrate that greater than 90% tumor SDMA reduction is required to achieve a maximal antitumor effect. However, tumor SDMA did not correlate well with tumor growth inhibition. To better understand the effects of AMG 193 on MTAP WT tissues, we evaluated blood SDMA levels. We observed dose-dependent SDMA inhibition in the blood that ranged from 29% to 73% inhibition (Fig. 4E). The level of SDMA inhibition in the blood was well correlated with percentage tumor growth inhibition ($R^2 = 0.9575$; Fig. 4F) and may provide a surrogate that is prognostic for the molecular tumor response and AMG 193 activity.

Next, we evaluated the effects of AMG 193 on endogenous MTAP-deleted CDX tumor models. AMG 193 was dosed at 10 to 100 mg/kg orally QD. Robust and statistically substantial antitumor activity was observed in a dose-dependent manner in DLBCL (DOHH-2), pancreatic (BxPC-3), and lung (LU99, H838) cancer CDX models (Fig. 4G; Supplementary Fig. S7C–S7E). In addition, PD and PK analysis
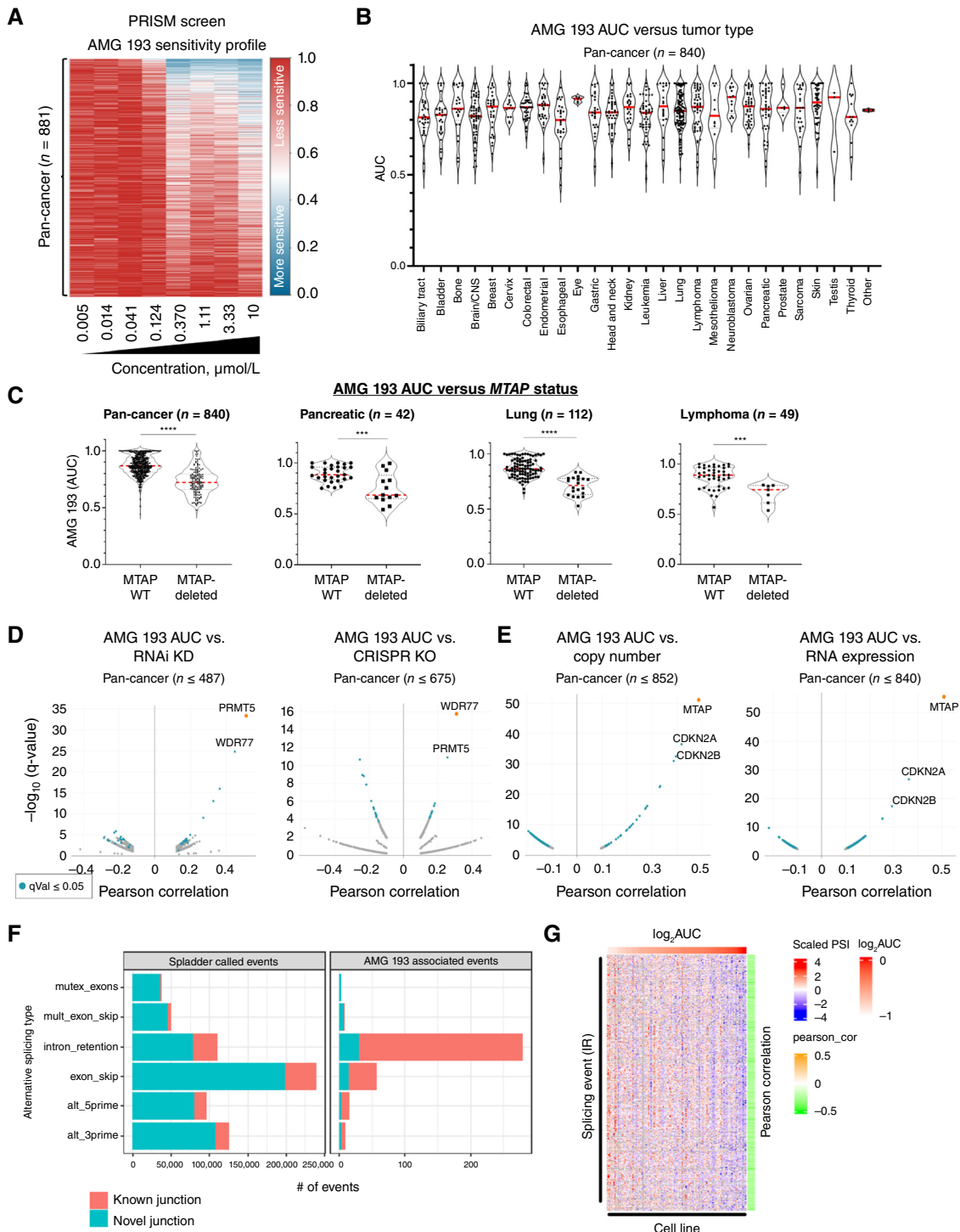
Figure 3. AMG 193 sensitivity profiling across a barcoded cancer cell line library. **A,** AMG 193 sensitivity profile shown by AUC across a panel of bar-coded cancer cell lines after 5 days of treatment with DMSO or AMG 193 (eight-point concentration range). Cell viability was determined by the relative abundance of each cell line barcode. **B,** AMG 193 AUCs *vs.* tumor lineage type. The red line indicates the average per group. **C,** AMG 193 AUC *vs.* MTAP status across all lineages, pancreatic, lung, or lymphoma. The dotted line indicates the average. **D,** AMG 193 AUC *vs.* RNAi knockdown (left) or CRISPR KO (right) for *PRMT5* and *WDR77* with the associated Pearson correlation value and *P*-value. **E,** AMG 193 AUC *vs.* copy number (left) or RNA expression (right) for *MTAP, CDKN2A,* and *CDKN2B* with the associated Pearson correlation value and *P*-value. **F,** AS events identified by SplAdder across all MTAP-deleted cell lines (left). AMG 193–associated AS events (right). One-side Fisher exact test $P < 2 \times 10^{-16}$. **G,** Heatmap showing Pearson correlations of intron re-tention events and $\log_2$AUC of AMG 193 across MTAP-deleted PRISM cell line panel. *, $P < 0.05$; **, $P < 0.01$; ***, $P < 0.001$; ****, $P < 0.0001$. AS, alternative splicing; CDKN2, cyclin-dependent kinase inhibitor 2; CRISPR, clustered regularly interspaced short palindromic repeats; KD, knockdown; KO, knockout; MTAP, methylthioadenosine phosphorylase; PRMT5, protein arginine methyltransferase 5; qVal, q-value; RNAi, ribonucleic acid interference; WDR77, WD repeat-containing protein 77; WT, wild-type.

Figure 4. AMG 193 inhibits the growth of MTAP-deleted tumors *in vivo*. **A,** SDMA ELISA analysis of HCT116 MTAP WT and MTAP-null bilateral tumors. Mice were administered a total of 4 doses, and tumors were collected 4 hours after the last dose. Percentage of inhibition reported relative to the matched vehicle. AMG 193 was quantified using LC-SRM MS methods for both plasma and tumor homogenate samples. Data represent mean ± SEM, $n = 5$ for each group. Statistical analysis by one-way ANOVA with Dunnett comparison to control; **, $P = 0.001$; ****, $P < 0.0001$. Mice with (**B**) HCT116 MTAP WT tumors and (**C**) HCT116 MTAP-deleted tumors were treated with AMG 193. **D,** Terminal HCT116 MTAP-deleted tumor SDMA analysis. **E,** Terminal blood SDMA analysis from mice bearing HCT116 MTAP-deleted tumors (from **C**). **F,** Correlation of HCT116 MTAP-deleted TGI (from **C**) to blood SDMA inhibition (from **E**). Performed simple linear regression analysis to determine R^2 value. **G,** Mice with H838 tumors were treated with AMG 193. **H,** Terminal H838 tumor SDMA analysis. **I,** Terminal blood plasma taken at 2, 4, 8, 16, and 24 hours after the last dose. Plasma taken from H838 CDX (**G**). The *in vitro* H838 IC_{50} is noted by the dotted line. PDXs (**J**) pancreatic tumors (**K**) lung tumors (**L**) melanoma tumors (**M**) esophageal tumors, were treated with AMG 193. CDX and PDX efficacy data and dosing regimen are as follows: mice were administered vehicle or AMG 193 PO QD for the duration of the study. Data represent group means ± SEM, $n = 10$. STATS: *P*-values were determined by linear mixed-effects model with a Dunnett comparison to control; ****, $P < 0.0001$. Terminal SDMA assessment in tumor (ELISA) and blood (flow cytometry) data represent mean ± SEM, $n = 5$ for each group. Statistical analysis by one-way ANOVA with Dunnett comparison to control; ****, $P < 0.0001$. CDX, cell line–derived xenografts; MTAP, methylthioadenosine phosphorylase; PDX, patient-derived xenograft; PO, orally; QD, daily; RLU, relative light unit; SDMA, symmetric dimethylarginine; SEM, standard error of the mean; TGI, tumor growth inhibition; TR, tumor regression; WT, wild-type.

demonstrated a reduction in the level of SDMA in tumor and dose-proportional plasma exposures in the H838 model, respectively (Fig. 4H and I; Supplementary Fig. S7F). The maximal tumor growth inhibition correlated with at least a 95% reduction in SDMA levels, confirming that near-complete PRMT5 inhibition may be required to achieve robust tumor growth inhibition in multiple preclinical models. To further understand the relationship between the exposure of AMG 193 and tumor growth inhibition, we compared the exposure of different doses of AMG 193 with coverage over the IC_{50} observed in an *in vitro* assay measuring the impact of AMG 193 on the viability of H838 cells [Fig. 1H (right)]. This analysis revealed that IC_{50} target coverage of at least 16 hours was required for maximal tumor growth inhibition, further supporting the relationship between prolonged and deep PRMT5 (SDMA) inhibition and antitumor efficacy. In summary, the preclinical pharmacology data highlight that high exposures of AMG 193 that drive sustained target coverage equating to complete or near-complete pharmacologic inhibition of PRMT5 will likely be required to replicate the synthetic lethal interaction observed between PRMT5 and loss of MTAP.

To examine the anticancer effects of PRMT5 inhibition more broadly, we used a panel of PDX models that more closely mirror the characteristics of human cancers and capture intratumor heterogeneity. A mouse clinical trial [HuTRIAL CrownBio (29–31)] was designed to evaluate the effects of PRMT5 inhibition across 25 MTAP-deleted PDX models that spanned eight different cancer types. AM-9747 was active in 17 of 25 (68%) MTAP-deleted PDX models demonstrated by greater than 50% tumor growth inhibition relative to the matched vehicle-treated tumors (Supplementary Fig. S7G; Supplementary Table S7). Based on the successful PDX mouse trial using AM-9747, we then evaluated the efficacy of AMG 193 against multiple PDX tumor models. AMG 193 treatment resulted in robust and statistically substantial antitumor activity in a dose-dependent manner in pancreatic, lung, melanoma, and esophageal PDX models (Fig. 4J–M). Overall, these *in vivo* data demonstrate that MTA-cooperative PRMT5 inhibitors AMG 193 and AM-9747 can inhibit MTAP-deleted tumor growth across a variety of tumor lineages.

Targeting MTAP-Deleted Cancer Cells via MTA-Cooperative PRMT5 Inhibition Results in Enhanced Tumor Killing While Sparing Healthy Normal Cells

First-generation PRMT5 inhibitors showed early promise of activity in patients, however, toxicity and limited antitumor response precluded further clinical development. We hypothesized that a molecule that selectively binds to PRMT5 in the presence of MTA would specifically target MTAP-deleted tumor cells resulting in increased potency and maximizing the therapeutic window. To evaluate this hypothesis, we used AM-9747 to establish a differentiated MOA compared with a noncooperative PRMT5 inhibitor (LLY-283) *in vivo*. Mice implanted with DLBCL (DOHH-2) tumors were sorted into three groups and dosed with either vehicle, LLY-283, or AM-9747 for the duration of the study.

Tumor volume measurements demonstrated that both inhibitors achieved a robust antitumor response, with the LLY-283 resulting in 2/10 tumor-free mice and AM-9747 resulting in 7/10 tumor-free mice (Fig. 5A). Treatment with AM-9747 was well tolerated by the mice for the duration of the study, with minimal decrease in body weights (Fig. 5B). To better understand the mechanisms governing the antitumor activity and the effects on normal cells after PRMT5 inhibitor treatment, we harvested a subset of tumors after 11 days of treatment. To determine the effects on the cell cycle, tumors were disaggregated, stained, and analyzed via flow cytometry. The cell cycle data showed a decrease in S-phase and G_2/M for both PRMT5 inhibitors; however, only AM-9747 treatment resulted in a substantial increase in the Sub-G1 population, indicating induction of cell death (Fig. 5C). To further understand on-target activity in tumor versus normal cells, we assessed SDMA levels in bone marrow, blood, and tumor via flow cytometric analysis. Treatment with the noncooperative inhibitor LLY-283 resulted in a pronounced decrease in SDMA levels in both the bone marrow (71%) and blood (79%). AM-9747 demonstrated substantially less SDMA inhibition in bone marrow (43%) and blood (54%) compared with LLY-283. Conversely, when measuring SDMA levels in the tumor, AM-9747 resulted in substantial SDMA inhibition (64%) compared with both vehicle and LLY-283 (21%; Fig. 5D). To further understand the effects of treatment on normal versus tumor tissue, we monitored the DNA damage marker γH2AX (phosphorylation of H2AX on serine-139). γH2AX levels were substantially induced in the bone marrow and blood when treated with LLY-283; however, minimal changes were observed with AM-9747 treatment (Fig. 5D). We next looked in the tumor compartment and observed substantial γH2AX induction when treated with AM-9747 and marginal changes with the noncooperative PRMT5i [Fig. 5D (right)]. Further analysis was conducted to understand the mechanism of toxicity observed with LLY-283. To this end, we analyzed the bone marrow progenitor populations from the above treated mice. We observed a substantial reduction in the megakaryocytic and erythroid progenitors (MEP) population when treated with LLY-283; however, the MEP population was unperturbed with AM-9747 treatment (Fig. 5E). Finally, because dose-limiting toxicities of first-generation PRMT5 inhibitors in the clinic included thrombocytopenia and anemia (16, 17), we evaluated the number of circulating blood cells in the mice after treatment. Treatment with LLY-283 resulted in highly substantial reductions in red blood cells (RBC), reticulocytes, and platelets (Fig. 5F). In contrast, AM-9747 did not affect levels of circulating blood cells after treatment. A follow-on study to support the preclinical development of AMG 193 was completed in mice bearing BxPC-3 xenografts. AMG 193 treatment did not affect circulating white blood cells and RBCs and had minimal decreases in reticulocytes and platelets when compared with vehicle-treated mice (Supplementary Fig. S8A). In addition, AMG 193 demonstrated robust tumor growth inhibition and no effects on body weight (Supplementary Fig. S8B and S8C). Together, these data suggest treatment with AMG 193 or AM-9747 drives substantial antitumor activity while sparing healthy normal cells.
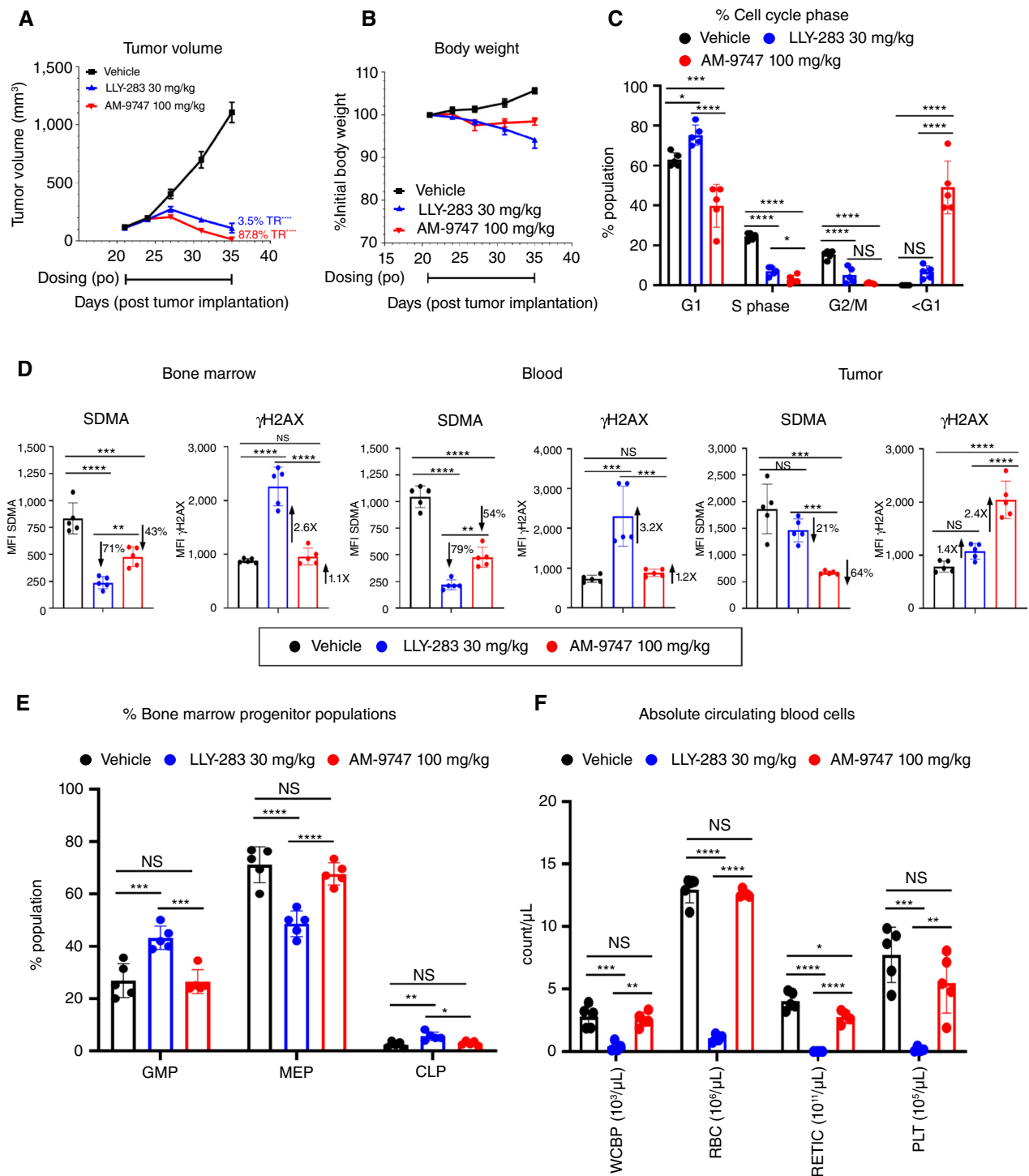
Figure 5. AM-9747 results in cell cycle arrest and an increase in the DDR in DOHH-2 tumors with no effect on circulating blood cells. **A–E,** Female SCID mice were implanted with DOHH-2 tumors. Once tumors reached ~115 mm³ mice were treated with either vehicle or AM-9747 at 100 mg/kg or noncooperative PRMT5i LLY-283 at 30 mg/kg. Mice were administered doses of PO QD for the duration of the study. A cohort of tumors was harvested on Day 11, and data represent group means ± SEM, n = 5. **A,** DOHH-2 tumor volumes. **B,** Mouse body weight. **C,** Disaggregated tumors were costained for DAPI and analyzed via flow cytometry. **D,** Bone marrow, blood, and disaggregated tumors were stained for SDMA or γH2AX. **E,** Bone marrow progenitor populations were stained and analyzed via flow cytometry. **F,** Cardiac bleeds were performed and analyzed on ADVIA. Statistical analysis by ordinary one-way ANOVA with Tukey multiple comparisons test. *, $P < 0.05$; **, $P < 0.01$; ***, $P < 0.001$; ****, $P < 0.0001$. γH2AX, phosphorylated histone H2AX; CLP, common lymphoid progenitor; DAPI, 4′,6-diamidino-2-phenylindole; DOHH-2, human B-cell lymphoma cell line; GMP, granulocyte-macrophage progenitors; MEP, megakaryocyte-erythrocyte progenitors; MFI, mean fluorescent intensity; NS, not significant; PLT, platelets; PO, orally; PRMT5i, protein arginine methyltransferase 5 inhibitor; QD, daily; RETIC, reticulocytes; SCID, severe combined immunodeficiency; SDMA, symmetric dimethylarginine; SEM, standard error of the mean; WBCP, white blood cell population.

AMG 193 Synergizes with SOC Chemotherapies and the KRAS G12C Inhibitor Sotorasib

Clinically, targeted cancer therapeutics are often combined with SOC chemotherapies to compliment or augment anticancer efficacy. To determine the potential for combination strategies with SOC agents, we performed *in vitro* synergy assays to assess the combination of AMG 193 with a panel of SOC chemotherapies representing a range of MOAs [paclitaxel, carboplatin, gemcitabine, irinotecan, 5-fluorouracil (5-FU), pemetrexed] in relevant cancer models. All SOC combinations evaluated exhibited some combination benefit, ranging from additivity to strongly synergistic (Fig. 6A). For one representative combination (AMG 193+carboplatin), *in vitro* synergy was confirmed by a left shift of the dose-response curve in viability assays, and a decrease in total nuclear counts over 10 days in the H292 NSCLC cell line (Supplementary Fig. S9A–S9D). One moderately synergistic (paclitaxel) and one strongly synergistic (carboplatin; Supplementary Fig. S9B) combination were evaluated further *in vivo*. In the H292 NSCLC xenograft model, both combinations resulted in greater tumor growth inhibition than either single agent (Fig. 6B and C). Both chemotherapy combinations were well tolerated *in vivo*, with no substantial body weight loss (Supplementary Fig. S9E). Mechanistically, carboplatin treatment augments the DNA damage induced by PRMT5 inhibition (Fig. 2D–F), resulting in higher levels of DNA damage after combination treatment, shown by increased γH2AX staining (Supplementary Fig. S9F and S9G). Cell cycle analysis also demonstrated that the carboplatin combination resulted in a greater decrease in S-phase and an increase in G_2/M cell populations relative to the PRMT5 inhibitor alone (Supplementary Fig. S9H). These data provide proof of concept for the utility of SOC combinations with MTA-cooperative PRMT5 inhibitors.

In addition to SOC chemotherapies, combination strategies with other targeted cancer therapeutics could be beneficial to patients whose tumors harbor both relevant genomic alterations. For example, approximately 2% to 3% of NSCLC are both MTAP-deleted and mutant for KRAS G12C (32), suggesting KRAS G12C inhibitors may provide an added benefit to PRMT5 inhibitors in this patient population. To study this hypothesis, we combined our MTA-cooperative PRMT5 inhibitors with the US Food and Drug Administration-approved KRAS G12C inhibitor sotorasib. *In vitro*, this combination is synergistic in the MTAP-deleted, KRAS G12C-mutant pancreatic line MIAPACA2 (Supplementary Fig. S10A and S10B) with combination index (CI) scores of <1. Additional studies with a combination of AM-9747 and sotorasib confirmed that the combination decreased the AM-9747 IC_{50} by 6.5-fold and decreased cell growth greater than either single agent (Supplementary Fig. S10C and S10D). In PDAC and NSCLC xenograft models harboring both genomic alterations (MIAPACA2 CDX, LU99 CDX, LU5268 PDX), combination treatment led to substantial tumor growth inhibition compared with either single agent (Fig. 6D–F). Importantly, no body weight loss was observed in these studies (Supplementary Fig. S10E). Immunoblots confirmed that combination treatment resulted in the inhibition of MAPK signaling, SDMA signaling, and protein kinase B (AKT)

signaling (Supplementary Fig. S10F). Cell cycle analysis revealed that the combination treatment augmented the G_1 arrest induced by sotorasib (Supplementary Fig. S10G). In summary, MTA-cooperative PRMT5 inhibitors can synergize with clinically relevant chemotherapies and targeted agents *in vitro*, and combination treatment *in vivo* substantially inhibits tumor growth.

AMG 193 Demonstrates RECIST Responses in Patients with MTAP-Deleted Solid Tumors

In the ongoing FIH study (NCT05094336), AMG 193 was evaluated in patients with homozygous loss of *MTAP* and/or *CDKN2A* (MTAP-deleted) solid tumors at escalating dose levels (33). Clinical activity was assessed every 8 weeks per Responses on the RECIST v1.1. Correlative molecular PD characterizations were performed, including longitudinal monitoring of circulating tumor (ctDNA/cTF) in the plasma and SDMA in the serum. On-treatment biopsies of tumor tissue were collected when feasible to evaluate target engagement by comparison of pre- and on-treatment tumor tissue by IHC for SDMA levels. The tumor methylation score obtained from the ctDNA was used to quantify the circulating tumor fraction (cTF) over time. Three individual case narratives were selected from responding patients from the ongoing clinical trial in which sufficient correlative biomarkers were available to inform proof of mechanism for AMG 193 in humans. MTAP deletions were established by next-generation sequencing (NGS) in the cases below.

A 55-year-old female with ovarian Sertoli–Leydig cell tumor was enrolled in the 20210023 clinical trial upon identification of homozygous *CDKN2A* and *MTAP* deletions by NGS. At diagnosis (16 months before enrollment), she underwent cytoreductive surgery followed by adjuvant platinum–based chemotherapy, but within 4 months her disease reoccurred requiring peritoneal cytoreductive surgery and need for further therapy. At the time of enrollment, she had three identifiable target lesions: a liver lesion (79 mm), a perirectal lymph node (50 mm), and a renal lymph node (13 mm). She received AMG 193 800 mg orally (PO) QD on a 28-day cycle. Her first on-treatment disease assessment at 8 weeks showed a 13% overall reduction in target lesions, which rose to a 48% overall reduction at 16 weeks, consistent with a RECIST-defined partial response. Each subsequent disease assessment continued to show an incremental reduction of target lesions with a nadir of 80% in cycle 17 (Fig. 7A). Serum SDMA dropped within the first week and stayed low with AMG 193 treatment (Supplementary Fig. S11A). She tolerated the treatment well and remains on study in cycle 19.

A 70-year-old female with pancreatic adenocarcinoma previously treated with pancreatectomy, splenectomy, and adjuvant FOLFIRINOX, gemcitabine/nab-paclitaxel, and nano-liposomal irinotecan–based chemotherapy was enrolled into the 20210023 clinical trial approximately 2 years after diagnosis. Homozygous *CDKN2A/MTAP* deletions, KRAS[G12R], and TP53[V157F] were detected by NGS. At the time of enrollment, she had multiple lesions in the liver and pancreatic neck; two liver lesions were identified as targets with an overall sum of 37 mm. She received AMG 193 1,200 mg PO QD on a 28-day cycle, which was well tolerated. The first on-treatment disease
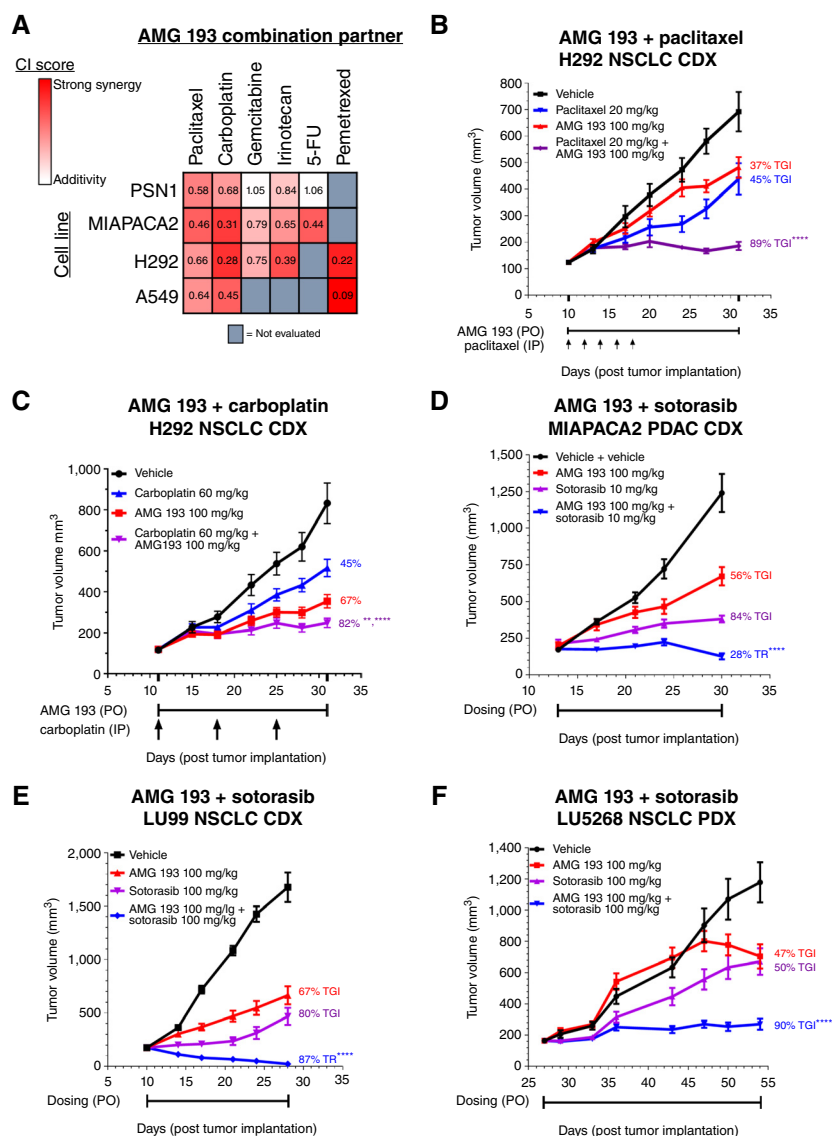
Figure 6. AMG 193 combination treatment with SOC chemotherapy or KRAS G12C inhibitor sotorasib significantly inhibits tumor growth in MTAP-deleted xenografts. **A,** Heatmap of minimum CI scores generated for AMG 193 combinations with indicated chemotherapies in a panel of cancer cell lines after 6 days of combination treatment. CI < 1 = synergy; CI = 1 = additivity; CI > 1 = antagonism (**B** and **C**) Female nude mice were implanted with H292 (NSCLC CDX) tumors. Vehicle and AMG 193 were administered PO QD for the duration of the study. **B,** Paclitaxel was administered IP starting on day 10 and then administered doses every other day for a total of 5 doses. **C,** Carboplatin was administered IP starting on day 10 and then administered doses weekly for a total of 3 doses. **D–F,** Female nude mice were implanted with MIAPACA2 (PDAC CDX) tumors, LU99 (NSCLC CDX) tumors, or LU5268 (NSCLC PDX) tumors, respectively, and vehicle, AMG 193 and sotorasib were administered PO QD for the duration of the study. Data represent mean ± SD, *n* = 10 for each group. *P*-values were determined by a linear mixed-effects model with a Tukey all-groups comparison, combination *vs.* either single agent; **, *P* < 0.01; ***, *P* < 0.001; ****, *P* < 0.0001. CDX, cell line–derived xenografts; CI, combination index; D, day; IP, intraperitoneally; KRAS, Kirsten rat sarcoma virus; MTAP, methylthioadenosine phosphorylase; NOD, nonobese diabetic; NSCLC, non–small cell lung cancer; PO, orally; QD, daily; SCID, severe combined immunodeficiency; TGI, tumor growth inhibition; TR, tumor regression.

assessment at 8 weeks showed an overall 46% reduction in target lesions, consistent with a partial response by RECIST, and nadir in target lesions of 49% at week 16. The carbohydrate antigen 19-9 (CA 19-9) decreased from 377 to a nadir of 37 kU/mL (90% reduction from baseline) in cycle 5. Serum SDMA dropped within the first week and stayed low with AMG 193 treatment (Supplementary Fig. S11B). She continues to receive AMG 193 1,200 mg QD in cycle 8 with ongoing RECIST response.

A 52-year-old male with squamous NSCLC harboring *MTAP* deletion and TP53$^{E286K/W146}$ was enrolled in the 20210023 clinical trial ~3.5 years after diagnosis. Before enrollment, he had received three lines of therapy in the metastatic setting, including platinum-based chemotherapy and pembrolizumab. At the time of enrollment, he had multiple lung lesions; two lung lesions were identified as targets with an overall sum of 34 mm. He received 800 mg AMG 193 PO QD on a 28-day cycle. The first on-treatment disease assessment showed a 26%
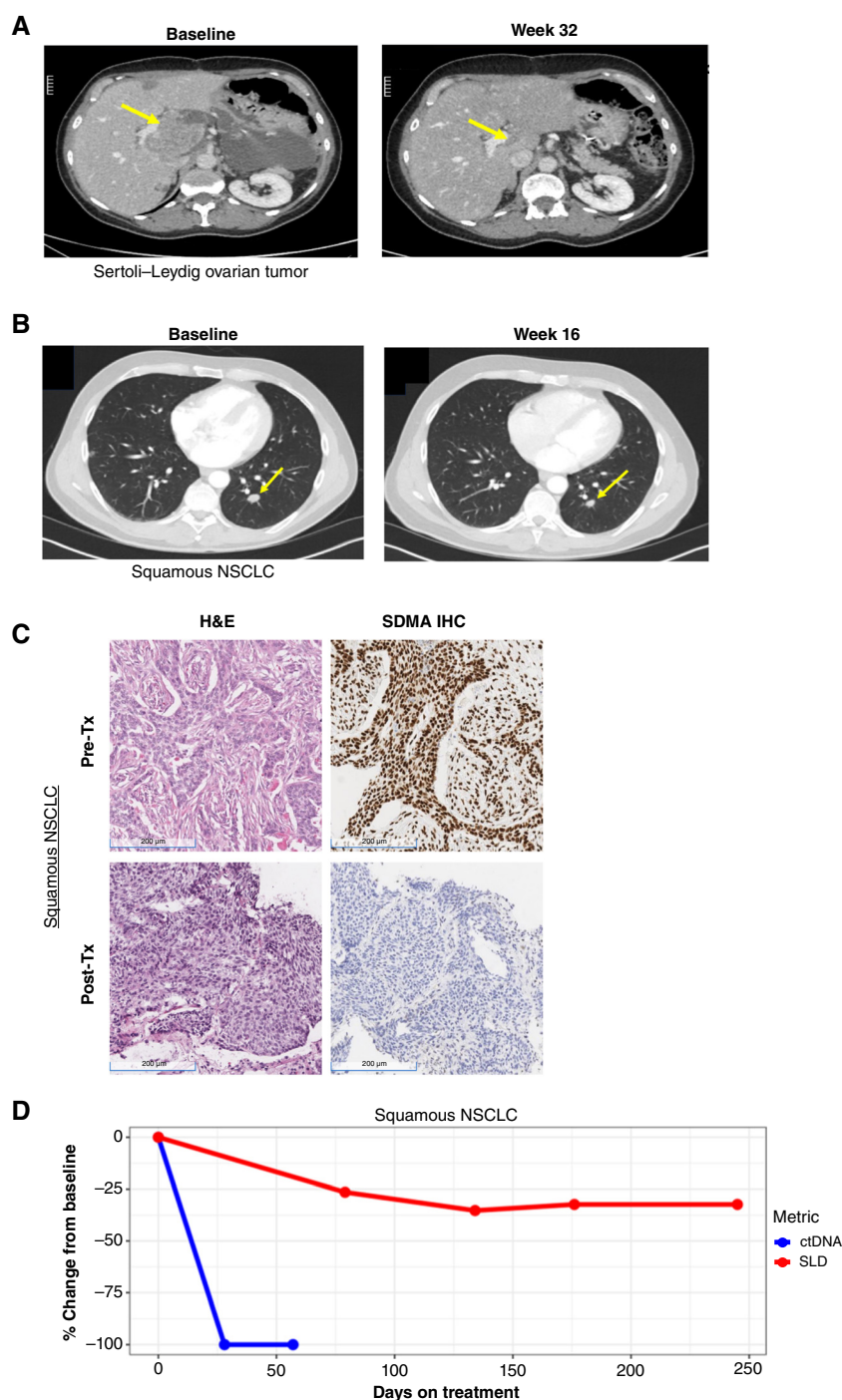
Figure 7. AMG 193 treatment in patients with MTAP-deleted cancers decreases tumor volume and plasma ctDNA levels. The measurements described in the figures are from central radiology review annotations. Tumor measurements and overall response assessments from central radiologists may be different from those described by the site investigator or radiologist. **A,** A patient with Sertoli–Leydig ovarian tumor with a liver lesion measuring 83.9×56.3 mm at baseline decreased to 31.3×18.0 mm at Week 32. **B,** Patient with squamous cell NSCLC with left lower lobe lung lesion measuring 16.4×12.3 mm at baseline decreased to 14.3×10.7 mm at Week 16. **C,** The inhibition of PRMT5-mediated SDMA modification in tumor biopsy of the patient with squamous NSCLC was observed after 1 month of treatment with AMG 193. Pretreatment and Cycle 2 Day 1 tumor biopsies were subjected to SDMA protein expression staining using IHC. Adjacent slides were also stained with H&E. The SDMA H-scores were determined by a pathologist. In the pretreatment (Pre-Tx) sample, all viable cells exhibited positive nuclear staining with an H-Score of 300. In the after-treatment (After-Tx) sample, no SDMA expression was detected in cancer cells, with an H-Score of 0. **D,** The monitoring of serial circulating tumor DNA levels utilizing the tumor methylation score for quantifying the tumor fraction in the patient with squamous NSCLC. The figure illustrates the time course of plasma levels of ctDNA (blue line) and imaging assessments expressed as sum of long diameter (SLD; red line) throughout the treatment. Levels of ctDNA are presented as the percentage of changes relative to the baseline. A ctDNA negativity response was observed after one cycle, and ctDNA negativity was sustained at Cycle 3 Day 1. ctDNA, circulating tumor deoxyribonucleic acid; H&E, hematoxylin and eosin; NSCLC, non–small cell lung cancer; PRMT5, protein arginine methyltransferase 5; SDMA, symmetric dimethylarginine.

overall reduction in target lesions, which reached a nadir of 35% reduction at 16 weeks, consistent with a partial response per RECIST (Fig. 7B). Biopsy of tumor tissue performed during cycle 2 showed a 100% reduction in SDMA (Fig. 7C). Serum SDMA and ctDNA/cTF declined within 1 and 4 weeks of starting treatment with AMG 193, respectively (Supplementary Fig. S11C; Fig. 7D). He remains on treatment beyond cycle 13, with 26% overall reduction relative to baseline and continues to receive AMG 193 800 mg QD.

DISCUSSION

In summary, AMG 193 is a novel MTA-cooperative PRMT5 inhibitor that selectively inhibits the growth of MTAP-deleted tumor cells in preclinical studies and shows promise as a clinical agent in early-phase clinical trials. AMG 193 was discovered through a novel DEL approach and was shown to bind potently and selectively to PRMT5 in a complex with MTA but not with SAM. Here, we demonstrated that MTAP-deleted cell lines are exquisitely sensitive to AMG 193 compared with MTAP WT in cell viability assays and demonstrated efficacy in a variety of human xenograft tumor models. Furthermore, in contrast to noncooperative PRMT5 inhibitors, our MTA-cooperative inhibitors have limited impact on normal bone marrow and blood cells, thus predicting tolerability clinically. Lastly, AMG 193 has shown safety and efficacy in the FIH clinical study with case studies of partial responses highlighted here.

AMG 193 represents a new class of PRMT5 inhibitors that uses the synthetic lethality of *MTAP* loss and accumulation of MTA in MTAP-deleted tumor cells. In contrast, the first-generation PRMT5 inhibitors were SAM-cooperative or SAM-competitive and indiscriminately inhibited PRMT5 in all cells leading to on-target toxicity in clinical trials (16). Because PRMT5 is a cell-essential protein and has clear roles in hematopoiesis, it is not surprising that global PRMT5 inhibition would lead to hematologic toxicity (34). However, the identification of PRMT5 as a synthetic lethal target opened the door for second-generation inhibitors to take advantage of the PRMT5:MTA complex in the MTAP-deleted setting, thereby broadening the therapeutic window. The DEL screen successfully identified a novel series of MTA-cooperative PRMT5 inhibitors that form a stable trimeric complex with PRMT5 and MTA but not with SAM. Optimization of the DEL hits led initially to a potent, selective, and orally bioavailable tool compound (AM-9747) that was extensively used to characterize this novel mechanism. Further multiparameter optimization guided by the cocrystal structure of AM-9747 complexed with the PRMT5:MTA complex resulted in the identification of our clinical candidate AMG 193. Unlike the first-generation inhibitors, this novel series does not impact the viability of normal WT cells, including the bone marrow progenitors and circulating blood cell populations. Another MTA-cooperative PRMT5 inhibitor MRTX1719 has shown similar findings in preclinical studies (10). MTA-cooperative PRMT5 inhibitors are an emerging class of therapeutics with several molecules entering the clinic (35, 36). MRTX1719 and AMG 193 structures reveal there are different ways to achieve MTA cooperativity through different PRMT5 binding modes. Early trial results with MRTX1719 also suggest tolerability and

safety, providing additional proof of concept to the clinical utility of MTA-cooperative PRMT5 inhibitors (10). In preclinical studies, intracellular MTA levels are reported to be ~2–15-fold higher in MTAP-deleted cells compared with MTAP WT cells (7–9). We do not understand how the levels of MTA in human tumors compare with those observed preclinically and if the absolute levels of MTA have the potential to predict clinical activity. However, the preliminary clinical efficacy and tolerability achieved with two MTA-cooperative PRMT5 inhibitors (AMG 193 and MRTX1719) suggest that MTAP-deleted tumors accumulate MTA and that a therapeutic window is achievable.

Here we demonstrate that *MTAP* loss is the top predictor of sensitivity to MTA-cooperative PRMT5 inhibitors. Furthermore, the use of homozygous deletion of *MTAP* as a clinical biomarker has been proven effective for enrolling patients in the ongoing clinical study. A key remaining question is whether there are additional biomarkers that can predict sensitivity or resistance to this new class of therapeutics. In the current study, comprehensive cell line profiling using the PRISM screen and associated DepMap datasets did not identify additional biomarkers. Besides *MTAP* loss, *CDKN2A/B* loss is the next predictor of sensitivity with no additional statistically substantial and reproducible genes found. The same is true for potential markers of resistance. Analysis of co-mutation frequency by others also has not elucidated alterations that cooccur with *MTAP* loss at a substantially higher frequency than in MTAP WT tumors (32). It remains to be seen from the clinical data if there are additional biomarkers that can be used to stratify patients. Preexisting splicing alterations or a baseline elevation of alternative splicing events may predict patients that are more sensitive to AMG 193 treatment, but further work is needed to fully evaluate this hypothesis. Intrinsic and acquired resistance frequently occurs with the treatment of targeted cancer therapeutics (37); therefore, it will be essential to monitor the clinical studies for the emergence of resistance and use this information to design rational combinations.

Combination strategies with AMG 193 are attractive for multiple reasons. First, overlapping hematologic toxicity is typically a major concern with chemotherapy combinations clinically. As AMG 193 is well tolerated at efficacious doses in murine models with no body weight loss and exhibits negligible effects on the hematologic compartment, we do not expect dose-limiting overlapping toxicities with SOC agents. We also anticipate a wider therapeutic index due to the high selectivity of AMG 193 for MTAP-deleted tumors. AMG 193 and SOC chemotherapies have complementary MOAs, with both impacting the DDR and inducing synergy *in vitro*. Additionally, combinations with other targeted agents like sotorasib provide an orthogonal approach that targets two independent pathways; thus, overlapping toxicity would be limited. Preclinically, a range of monotherapy responses were observed across indications. Although the reason for this range in response is still undetermined, combination strategies that potentiate the activity of AMG 193 could provide a clinical benefit. Here, we demonstrated proof of concept of this strategy with a variety of combination treatments (carboplatin, paclitaxel, and sotorasib) which resulted in increased tumor growth inhibition in several CDX and

PDX models, setting the foundation for clinical exploration of AMG 193 in combination with SOC chemotherapies or targeted agents.

AMG 193 was the first MTA-cooperative PRMT5 inhibitor to enter the clinic. In the ongoing FIH study presented herein, encouraging preliminary antitumor activity has been observed in a variety of solid tumors, including NSCLC, pancreatic, renal cell carcinoma, ovarian Sertoli–Leydig cell tumor, gallbladder, and esophageal. This is in line with the preclinical evidence in PDX and CDX models of AMG 193 activity across an array of tumor indications, including lung, pancreatic, and esophageal. The high prevalence of *MTAP* deletion in patients presents a vulnerability to exploit synthetic lethality in selected indications with AMG 193. It remains to be seen whether particular indications are more sensitive to AMG 193 clinically; signal seeking in defined MTAP-deleted tumors is underway. Preliminary clinical safety findings (absence of cytopenia) are consistent with the high selectivity of AMG 193 for MTAP-deleted tumors over healthy tissues. This is in contrast to first-generation PRMT5 inhibitors in which clinical development was limited by the occurrence of cytopenias, such as thrombocytopenia and anemia. Furthermore, the serum SDMA data indicate stable target inhibition over time and demonstrate the utility of serum SDMA measurements to assess AMG 193 activity in clinical samples. AMG 193 in combination with chemotherapy or immunotherapy is currently under investigation in ongoing clinical trials in patients with lung, pancreatic, or biliary tract cancers (NCT06333951 and NCT06360354). Encouraging antitumor activity observed clinically may be augmented with SOC therapies for these indications.

METHODS

Cell Lines

Tumor cell lines were obtained from commercially available sources, including the ATCC, Japanese Collection of Research Bioresources, and German Collection of Microorganisms and Cell Cultures. HCT116 WT and MTAP-deleted cells were purchased from Horizon discovery (HD PAR-034, HD R02-033). MIAPACA2 and H838 cells used were *in vivo* passaged twice for better tumor growth kinetics. All cell lines were cultured in ATCC-, German Collection of Microorganisms and Cell Cultures–, or Japanese Collection of Research Bioresources–recommended growth media containing 10% FBS, except when specified. All cell line cultures were maintained at 37°C in an atmosphere of 5% CO_2 and cultured for 1 to 2 weeks prior to use in experiments. Authentication of cell lines was performed with short-tandem repeat DNA typing by ATCC, LapCorp, or IDEXX BioAnalytics between May 2018 and July 2024. Using an RT-PCR-based assay, all cell lines used for *in vivo* studies were tested for *Mycoplasma* contamination before use.

Small Molecule Compounds

Compounds were procured from commercial sources [carboplatin, gemcitabine, pemetrexed, irinotecan, 5-FU (Selleck), and paclitaxel (Sigma-Aldrich)]. PRMT5 compounds (AMG 193, AM-9747, EPZ015666, and LLY-283) and sotorasib were synthesized by Amgen.

Viability Assays

Cells were seeded at optimized densities in 96-well tissue culture plates, incubated overnight at 37°C in 5% CO_2, and treated with a nine-point serial dilution of AMG 193 or AM-9747 using a top concentration of 10 µmol/L (or 1 µmol/L for AM-9747 in the DLBCL lines), 1:3 serial dilution steps, and a DMSO-only control in triplicate. Following compound treatment for 6 days, effects on cell viability were measured with the CellTiter-Glo viability assay (Promega) as follows: treated cells and CellTiter-Glo luminescent cell viability assay reagents (Promega) were allowed to equilibrate to room temperature (RT), and 100 µL aliquots of reconstituted CellTiter-Glo reagent were added to each well of drug-treated cells. Assay plates were shaken for 2 minutes followed by incubation at RT for 10 minutes. Plates were then read on an EnVision Multilabel Reader. Percent of control (POC) values were calculated as follows: POC = 100 × (Treatment/Vehicle). Mean POC values were then calculated for each treatment condition and used to fit the dose-response curves, applying a four-parameter logistic curve in GraphPad Prism to determine the IC_{50} for each cell line. For those cell lines in which the dose-response curves did not reach 50% inhibition, the IC_{50} values are noted as >10 µmol/L. Assays were performed in triplicate in at least two independent experiments.

Immunoblot Analysis

Treated cells were collected and lysed in RIPA lysis buffer containing appropriate phosphatase and protease inhibitors (Thermo Fisher Scientific). Lysates were rotated for 30 minutes at 4°C, then precleared via centrifugation at 4°C, followed by analysis using Pierce BCA protein assay (Thermo Fisher Scientific) to determine protein concentration. Per the manufacturer's recommendation, 20 to 35 µg of lysates were resolved on NuPAGE gels (Life Technologies) and transferred to polyvinylidene difluoride membranes (Life Technologies), which were blocked in tris-buffered saline +5% milk and probed with indicated primary antibodies in Supplementary Table S8. Membranes were then incubated with secondary anti-species antibodies conjugated to horseradish peroxidase (GE Healthcare). SuperSignal West Pico, West Dura, or West Femto Chemiluminescent Substrates (Thermo Fisher Scientific) were used to develop a horseradish peroxidase signal, which was captured with a ChemiDoc imaging system (Bio-Rad).

Barcoded Cancer Cell Line Screen

AM-9747 was screened using PRISM barcoded cancer cell line collection established by the Broad Institute (www.theprismlab.org). Cell line pools (n = 20–25 cell lines per pool) were treated with AMG 193 over an 8-point concentration range (top concentration of 10 µmol/L, threefold dilution) for 5 days in triplicate wells, bortezomib (20 µmol/L) and DMSO were used as positive and negative controls, respectively. Viability curve-fitting and AUC value determination were performed for individual cancer cell lines as previously outlined (26, 27). Cancer cell lines with reported AMG 193 AUC values were selected for association analysis performed using the Cancer Dependency Map (DepMap.org) Consortium custom tools (dataset releases 22Q2 and 23Q2). Pan-cancer cell line data were graphed as either AMG 193 concentration–response heatmap or as AMG 193 AUC versus tumor-type violin plot. Pan-cancer AMG 193 AUC scores were correlated (Pearson correlation) with RNA expression, copy number, or gene dependency scores using either Combined RNAi (Broad, Novartis, Marcotte) or CRISPR (Avana) datasets. Computed correlation values and associated *P*-values and/or *q*-values were assigned for individual gene dependencies and graphed as volcano plots. Pan-cancer or lineage-specific AMG 193 AUC values were graphed based on MTAP expression. MTAP-deleted cell lines were identified based on a weighted copy number ratio of <0.4 and a gene expression $\log_2$ (TPM+1) value <1.6. TPM = transcripts per million

In Vitro Combination Studies

Cancer cell lines were treated with the combination of AMG 193 or AM-9747 and a combination partner (sotorasib, carboplatin, paclitaxel, irinotecan, 5-FU, pemetrexed, gemcitabine) for 6 days in duplicate. AMG 193/AM-9747 was performed at a 1.9-fold dilution

series and the combination partner was performed at a 1.2 to 1.7-fold dilution series to create an 8 × 10 dose matrix including DMSO-only controls. Cell viability was measured by the CellTiter-Glo Luminescence assay as in the single-agent viability assays. Raw luminescent values were converted to fraction affected (Fa) with the following equation: Fa = 1 − (treatment/average of DMSO-only wells). Synergy analysis was performed using the CalcuSyn software (Biosoft, v2.11) to determine CI scores based on the drug concentrations used and corresponding Fa values. CalcuSyn uses the Chou-Talalay method for drug combinations (38). Heatmaps show the calculated CI scores across the dose matrix. Assays were performed in duplicate in at least two independent experiments. Supplementary Figures S9B and S10B represent one representative study. To assess cell growth after combination treatment, nuclear counts were performed on the IncuCyte live cell imager (Sartorius) over 8 to 10 days using the NucLight Rapid Red Dye (Sartorius) in 10 wells/condition.

Cell Cycle Analysis

Cells were seeded in six-well plates at optimized cell densities for 4- or 6-day cell readouts and cultured overnight. For single-agent studies, cells were treated with 100 to 200 nmol/L AM-9747 or 10 μmol/L EPZ015666. For combination studies, cells were treated with DMSO or AM-9747 (0.15 μmol/L), sotorasib (0.05 μmol/L), carboplatin (3 μmol/L), or relevant combinations. After 4 or 6 days, cells were pulsed with bromodeoxyuridine (BrdU; Invitrogen) for 2 hours before cell harvest, fixed in methanol (90%), acid-washed in 2N HCl for 1 hour, and neutralized with wash buffer (1 × PBS, 0.1% Triton X-100, 1% BSA) in preparation for staining with anti-BrdU-AlexaFluor-647 (B35140, Invitrogen, RRID:AB_2536440) antibody and stained with 4′,6-diamidino-2-phenylindole (DAPI) and processed for flow cytometry–based cell cycle analysis. Cells were analyzed on BD LSRFortessa flow cytometer running BD FACSDiva software (BD Biosciences).

High-Content Imaging

Cell lines were seeded in 96-well plates at densities optimized for 4- or 6-day cell growth assays. The next day, cells were treated with DMSO or AMG 193/AM-9747. After 4 days of treatment for DDR proteins, cells were fixed with 4% formaldehyde (Thermo Fisher Scientific), washed with PBS, and permeabilized in wash buffer [PBS, 1% BSA (Thermo Fisher Scientific), 0.2% Triton X-100 (Sigma-Aldrich)]. Cells were stained in wash buffer with primary antibodies at 1:800 (p-Histone H2AX-S139, Millipore Clone JBW301, mouse, RRID:AB_309864; p21, Cell Signaling #2947, rabbit, RRID:AB_823586) for 2 hours at RT. Cells were washed three times in wash buffer and stained with secondary antibodies [anti-mouse-IgG-AlexaFluor-568 (A11004, Invitrogen, 1:2,000, RRID:AB_2534072), anti-rabbit-IgG-AlexaFluor-488 (A11034, Invitrogen, 1:2,000, RRID:AB_2576217), anti-rabbit-IgG-AlexaFluor-647 (A21245, Invitrogen, 1: 2,000, RRID:AB_2535813)] and Hoechst 33342 (Invitrogen) DNA dye and incubated for 1 hour at RT. Cells were washed three times and left in PBS for imaging. Images were captured in 32 fields per well using the ArrayScan VTi HCS Reader (Thermo Fisher Scientific) or the CellInsight CX7 Pro HCS Platform with a 10× objective. The total number of valid nuclear objects (mean object area ±3 SD based on DMSO control) was counted for each well. β-Galactosidase staining was performed after 6 days of drug treatment using the CellEvent Senescence Green Detection Kit (Invitrogen). The manufacturer's protocol was used except that the incubation with the CellEvent reagent was done at 1:500 for 4 to 6 hours.

Differential Expression Analysis with RNA-Seq

Raw RNA-seq reads were preprocessed with fastp (v 0.19.8) and quantified by SALMON (v 0.13.1) using Omicsoft-processed gene model Human.B38_OmicsoftGencode.V33 as reference. The transcript-level count matrix was imported to R (v4.0.2) with package tximport (v 1.22.0) and converted to a gene-level count object through package DESeq2 (v 1.34.0). Differential expression analysis was performed by fitting a generalized linear model against treatment (AM-9747 vs. DMSO control) with cell line as covariate (approximate treatment + cell_line). The substantially differential expressed genes (DEG) were defined as FDR < 0.05 and absolute fold change (FC) >1.5. The treatment DEGs were further filtered to ensure maximum condition mean FPKQ >1 for all cell lines. Finally, 1803 treatment DEGs were identified to be differentially expressed in response to IC50 AM-9747 in three pancreas cell lines. These DEGs ranked by log_2FC were further used for gene set enrichment analysis in Gene Ontology (GO.db v3.14.0), Reactome (ReactomePA v1.38.0), and Wikipathway (20220710) with R package clusterProfiler (v4.2.2). The enrichment significance was defined as FDR < 0.1, and the top 10 enriched pathways were plotted using ggplot2 (v 3.4.2).

Alternative Splicing Analysis with RNA-Seq

Alternative splicing analysis was mainly performed by SplAdder (v3.0.3; ref. 39). First, the raw RNA-seq reads were aligned to human GRCh38 gene model gencode V38 using hisat2 (v 2.2.0) by suppressing discordant alignments for paired reads (–no-discordant). The alignment was passed to create an individual splicing graph per input sample (spladder build–merge-strat single–no-extract-ase). Then, all individual graphs were merged into a joint–graph representation–(spladder build–merge-strat merge_graphs–no-extract-ase), and edges and nodes in the joint graph were quantified for each individual input sample (spladder build–merge-strat merge_graphs–no-extract-ase–quantify-graph-qmode single). Six types of events (exon skipping, intron retention, alternative 3′ splice sites, alternative 5′ splice sites, mutual exclusive exons, and multiple exon skips) were quantified from the previous graph quantification. To identify the AM-9747-associated alternative splicing events, AM-9747-treated samples were compared with DMSO control within each cell line using the test mode of SplAdder. Significant alternative splicing events in response to AM-9747 were defined as FDR < 0.05, and effect direction was determined by delta percent spliced-in. The genes under substantial alternative splicing in response to AM-9747 were further used for gene set over-representative analysis in Gene Ontology, Reactome, and Wikipathway with R package clusterProfiler. The enrichment significance was defined as FDR < 0.1, and the top 10 enriched pathways were plotted using ggplot2.

To investigate the association between alternative splicing rate and sensitivity to AMG 193 *in vitro*, we compiled a splicing atlas for MTAP-deleted cell lines using publicly available RNA-seq data from the Cancer Cell Line Encyclopedia (28). MTAP-deleted cell lines were identified based on a weighted copy number ratio of <0.4 and a gene expression $log_2(TPM+1)$ value of <1.6. Among these, 129 MTAP-deleted cell lines were detectable in PRISM screens and were accessible through the bio project PRJNA523380, which we leveraged to construct the MTAP-deleted splicing atlas (Supplementary Table S5). Six types of splicing events were identified using SplAdder, as outlined previously. The percent spliced-in value was then obtained for each event and correlated with the log_2AUC values of AMG 193 across 129 MTAP-deleted cell lines in the PRISM screen. Significant AMG 193-associated events were determined by adaptive shrinkage *q*-value of <0.05, a sample size of ≥50, and an absolute correlation coefficient value of ≥0.2 (Supplementary Table S6). The enrichment of event type among AMG 193-associated splicing events was investigated using a one-sided Fisher exact test.

Comet Assays

Comet Assays were performed per the manufacturer's recommendations (R&D Systems #4250-050-ESK).

SPR Assays

Small molecule direct-binding and chaser-binding assays were characterized with SPR technology using Biacore 8000 Cytiva Instruments. For biosensor surface preparation, the first step of SPR assays involved immobilization of a functional and stable biosensor surface with recombinantly expressed and purified biotinylated PRMT5-MEP50 complex. Target immobilization experiments were carried out at 25°C in a running buffer containing 0.01 mol/L HEPES pH 7.4, 0.15 mol/L NaCl, 0.005% v/v Surfactant P20 buffer with 1 mmol/L (TCEP), filtered, degassed. NeutrAvidin–Biotin capture surface was prepared on CM5 Series S sensor chips (Cytiva BR100530) with amine coupling using N-hydroxysuccinimide (NHS) and N′-(3-dimethylaminopropyl) carbodiimide hydrochloride (EDC). Carboxymethyl dextran surface was activated with EDC/NHS injections for 420 seconds at a flow rate of 10 μL/minute followed by immobilization of NeutrAvidin (Thermo Fisher Scientific) diluted to 40 μg/mL in acetate buffer (pH 5.5). NeutrAvidin amine coupling resulted in typical immobilization levels of 8,000 to 10,000 response units (RU) on both flow cells 1 and 2. The surface was deactivated using Ethanolamine-HCl for 7 minutes at a flow rate of 10 μL/minute. Surface was regenerated with 1 mol/L NaCl– 10 mmol/L NaOH for 1 minute at 50 μL/minute. Biotinylated PRMT5-MEP50 proteins were then captured at 1 μmol/L and stabilized on all eight channels of flow cell 2. Only injection for 10 to 20 minutes at 1 μL/minute resulted in capture levels ranging from 2,000 to 4,000 RU.

For the PRMT5 small molecule binding assay, binding experiments were carried out in 0.01 mol/L HEPES pH 7.4, 0.15 mol/L NaCl, 0.005% v/v Surfactant P20, 1 mmol/L TCEP, 1% DMSO ± 20 μmol/L MTA or SAM filtered, degassed. Small molecule binding SPR assays were optimized with either multicycle kinetics or single-cycle kinetics injection types depending on the kinetics of interactions. For affinity calculations, 7 to 11 concentrations of small molecule analytes ranging from 0.1 to 100 nmol/L (twofold dilution) were flowed over immobilized protein at a flow rate of 50 μL/minute, with an association phase of 300 seconds and dissociation phase of 2,100 seconds in multicycle kinetics. Data were solvent-corrected and double-referenced by Biacore Insight Software. Corrected data were fitted globally or locally to a 1:1 binding affinity and kinetic interaction model and the $K_{D(Kinetics)}$ values were determined from the (k_d/k_a) ratio. Binding equilibrium constants $(K_D)_{(Steady\ State)}$ were also inferred from the steady state binding curves and the maximum observed RU levels when applicable. To compare the binding results in RU between various experiments, analyte concentrations, or cycles, SPR data were normalized by correcting variations in PRMT5 capture levels and according to the molecular weight of the analytes and target. R_{max} (theoretical maximal binding at saturation of the analyte) was calculated with the following equation:

$$RMax\ (RU) = \left(\frac{MW\ of\ Analyte}{MW\ of\ Target} \right) \times Target\ Capture\ Levels\ (RU) \times stoichiometry$$

where MW is the molecular weight of the protein captured to the chip (target) and the small molecule injection over the captured target (analyte). This is corrected with the stoichiometry (considered 1:1 for PRMT5-SM inhibitors) of the binding between the analytes and the amount of target immobilized on to the chip surface measured as RU. After R_{max} was established for each run, the level of binding was captured as binding surface occupancy or percentage of R_{max} and calculated with the following equation:

$$\%\ RMax\ (RU) = \left(\frac{Observed\ Maximum\ Binding\ Responses\ (RU)}{RMax} \right) \times 100$$

where the observed maximum binding response is a measured parameter immediately after the end of the injection of the analyte and expressed in RU.

Chaser-Binding Assay

To experimentally calculate the kinetics, affinity, and in vitro half-life $(t_{1/2})$ for AMG 193, we applied a method referred to as "SPR chaser assay." This is a lower throughput SPR assay that provides a residence time of up to a few days, extremely slow off rates $(k_d < 1e{-}4$ per second), and up to single-digit pM sensitivity for highly stable target ligand captured complexes on the biosensor surface (22). The chaser assay was performed on a Biacore 8000+ (Cytiva) instrument at 25°C. Streptavidin (SA) capture surface was prepared on a biosensor Biotin CAPture chip with SA-bound single-stranded oligo (Cytiva) on both channels 1 (reference) and 2 (sample); 0.01 mol/L HEPES, pH 7.4, 0.15 mol/L NaCl with 0.005% v/v Surfactant P20, 1 mmol/L TCEP, 1% DMSO ± 20 μmol/L MTA or SAM buffer was used for sample preparations, as well as running the chaser assay. Bio-PRMT5-MEP50 was preincubated with AMG 193 with saturating concentration (ratio 1:10) to ensure complete saturation and formation of PRMT5-MTA-AMG 193 complex. Bio-PRMT5-MEP50-MTA-AMG 193 complex was captured on the SA surface at a concentration of ~20 to 100 μg/mL with a flowrate of 2 μL/minute with capture levels ranging from 2,000 to 4,000 RU on channel 2 and all flow cells 1 to 8. Furthermore, 100 nmol/L of AMG 193 was injected into flow cell 2 for 10 minutes at the flow rate of 30 μL/minute to ensure further binding saturation on surface-bound PRMT5-MTA complex with AMG 193. Chaser molecule 2 was then injected at 1 μmol/L on all flow cells with AMG 193 and a blank reference at the flow rate of 50 μL/minute at 0, 1, 3, 6, 9, 15, 21, 27, 33, 39, 45, 51, 57, and 64 hours. Association and dissociation time was kept at 180 and 600 seconds, respectively.

To experimentally observe all binding responses for the chaser molecule at various time points, data (repeated four times) was processed and analyzed by Biacore Insight Evaluation Software (Cytiva) and responses were transferred to Excel to calculate the percentage dissociation of AMG 193. The binding of chaser molecule to PRMT5+MTA+Inhibitor AMG 193 complexes was normalized to binding of chaser to (inhibitor unbound) blank reference PRMT5-MTA and calculated as percentage binding versus time for injections. The percentage bound was calculated by subtracting chaser binding from 100% (21).

% binding of chaser

$$= \left(\frac{[RU\ of\ chaser\ to\ PRMT5 + MTA] - [RU\ of\ PRMT5 + MTA + AMG\ 193\ complex]}{RU\ of\ chaser\ to\ PRMT5 + MTA} \right)$$
$$\times 100\%$$

The k_d and $t_{1/2}$ were determined in GraphPad Prism version 8 by fitting into the one-site exponential decay function, $Y = Y_0 \times \exp(-K \times X)$. Association rate (k_a) and binding affinities (K_D) were subsequently calculated from the chaser assay–derived k_d as a fixed value in the Langmuir 1:1 kinetic model with single-cycle kinetic sensorgrams collected in the direct-binding assay for AMG 193 and PRMT5+MTA complex on the surface.

Protein Expression and Purification

Protein for X-ray crystallography was recombinantly expressed in a baculovirus expression system according to literature procedures (40). Protein purification was conducted at 4°C unless specified. Frozen cell pellets from co-expression of PRMT5 and MEP50 were resuspended in lysis buffer [50 mmol/L HEPES pH 7.5, 300 mmol/L NaCl, 10% (v/v) glycerol, 1 mmol/L TCEP, 0.1% (v/v) Triton X-100], and the homogenous cell suspension was lysed by passing twice through microfluidizer; the lysate was clarified by centrifugation at 235,000 × g for 60 minutes. The supernatant after centrifugation was filtered through cheesecloth and a 0.2 mm membrane filter to remove any further particulates, which clarified the supernatant subject to Ni IMAC purification. After washing the NiExcel resin with wash buffer (lysis buffer + 20 mmol/L imidazole pH 8.0), the bound PRMT5-MEP50 complex was eluted using a linear gradient from 20 to 300 mmol/L imidazole pH 8.0 in elution buffer (50 mmol/L HEPES pH 7.5,

300 mmol/L NaCl, 1 mmol/L TCEP). Fractions containing PRMT5-MEP50 were subject to tobacco etch virus protease (1:100) cleavage overnight in dialysis membrane (Por, 12,000–14,000 Da) in dialysis buffer (50 mmol/L Tris pH 7.5, 50 mmol/L NaCl, 20% glycerol, 1 mmol/L TCEP). The tobacco etch virus cleaved PRMT5-MEP50 complex was diluted twofold in MonoQ buffer (20 mmol/L Bis-Tris pH 6.3, 10% glycerol, 1 mmol/L TCEP) and pH adjusted to an approximate pH of 6.5 using 1 mol/L Bis-Tris pH 6.3 stock solution. The cleaved protein was subjected to anion exchange purification. After binding, the column was thoroughly washed with MonoQ buffer and bound PRMT5-MEP50 was eluted using a linear 40 CV gradient from 0 to 1 mol NaCl in MonoQ buffer. The fractions containing >90% pure protein were pooled and concentrated to 5 mg/mL, and size exclusion chromatography was performed on a Superdex S200 column in SEC buffer (50 mmol/L Tris pH 7.5, 500 mmol/L NaCl, 10% glycerol, 1 mmol/L TCEP). Ultrapure PRMT5-MEP50 eluted as a single homogenous and symmetric peak. The peak fractions were pooled and concentrated to 13.5 mg/mL, aliquoted, and flash-frozen in liquid nitrogen and stored at −80°C for crystallization experiments.

Crystallization, Data Collection, and Cocrystal Structure Determination for AMG 193

PRMT5-MEP50 protein complex at 13.5 mg/mL was mixed with SFG in a 1:1.2-M excess ratio of SFG in 50 mmol/L Tris pH 7.5, 500 mmol/L NaCl, 10% glycerol, and 1 mmol/L TCEP and incubated on ice for 15 minutes before crystallization set-up. Protein crystallization was performed using the sitting drop vapor diffusion technique in 96-well trays using Mosquito. Crystals of the PRMT5-MEP50_SFG complex grew at 4°C from a 1:1 mix of this protein complex in 0.1 mol/L Na citrate tribasic dihydrate pH 5.6 buffer containing 2% Tascimate pH 5.0% and 16% PEG 3350 as precipitant over a period of 1 to 2 weeks. Before data collection, the crystals were soaked in a 1:1 M ratio mixture of AMG 193 and MTA in mother liquor supplemented with 20% glycerol as a cryoprotectant for 30 minutes at RT. The soaked crystals were harvested and flash-frozen in liquid nitrogen at 100 K for data collection.

Multiple crystals were screened for diffraction and the best diffracting crystals were picked. Diffraction data for AMG 193 complexed MTA-PRMT5-MEP50 crystals were collected on a Dectris Pilatus 6 mol/L silicon pixel detector at the Advanced Light Source Beamline 5.0.2 at wavelength 1.00000 Å and temperature 100 K. The data were integrated and scaled using HKL2000 (40). The structure was solved by molecular replacement with Phaser (41) from the CCP4 program suite using 4GQB with ligands removed as a search model (42). Model building was completed using COOT (42) based on sigma-A–weighted 2|Fo|−|Fc| and |Fo|−|Fc| electron density maps with iterative cycles of refinement using Phenix (43). The final structure of PRMT5-MEP50 in complex with MTA and AMG 193 was determined at 2.85 Å (Supplementary Table S2).

Ethics Statement

All animal experimental protocols were approved by the Amgen Institutional Animal Care and Use Committee and were conducted in accordance with the guidelines set by the Association for Assessment and Accreditation of Laboratory Animal Care. Mice were housed in an environmentally controlled room (temperature 23°C ± 2°C, relative humidity 50% ± 20%) on a 12-hour light/dark cycle. Mice were fed commercial rodent chow and water ad libitum. Mice with a tumor size exceeding 2,000 mm³ were removed from the study and euthanized. The clinical study NCT05094336 was conducted in accordance with the ethical principles derived from international guidelines including the Declaration of Helsinki, Council for International Organizations of Medical Sciences International Ethical Guidelines, and applicable International Conference on Harmonization Good Clinical Practice Guidelines. The study protocol was approved by an institutional review board/independent ethics committee at each study site, and patients provided written informed consent.

In Vivo Pharmacology

Mice were housed in sterilized filter-capped cages and maintained under aseptic and pathogen-free conditions. All studies used female 4- to 8-week-old athymic nude, CB17 SCID mice (Charles River Laboratories) or NOD/SCID mice (Jackson Laboratories). AMG 193 was formulated in 2% hydroxypropyl methylcellulose and 0.1% Tween-80 at pH 2.0. AMG 193 was stored at 2°C–8°C and protected from light. AMG 193 was mixed well before PO administration.

Tumor dimensions were assessed twice weekly with a Pro-Max electronic digital caliper (Japan Micrometer Mfg. Co. LTD.), and tumor volume was calculated using the formula length × width × height and expressed as mm³ using StudyDirector. Body weight was measured twice per week using an analytical laboratory scale.

The percentage of tumor growth inhibition (%TGI) was calculated as %TGI relative to the vehicle alone: %TGI = 100 − [(Treated − Initial Volume)/(Control − Initial Volume) × 100]. The percentage of tumor regression (%TR) was calculated as %TR of final tumor volume compared with the initial tumor volume: %TR = 100 − [(Final Volume)/(Initial Volume) × 100]. Tumor efficacy data expressed as mean tumor volume ± SEM for each group was plotted as a function of time (days).

HCT116 MTAP WT/Deleted Pharmacodynamic Assay

Athymic nude mice were implanted bilaterally with HCT116 MTAP WT and HCT116 MTAP-deleted cells (2.0E + 06 with Matrigel). Animals with established tumors were sorted into groups (n = 5) with similar tumor volumes (range, 250–450 mm³). Animals were administered vehicle or AMG 193 (3, 10, 30, 100 mg/kg) PO QD for 4 days. Tumor and blood plasma samples were collected 4 hours after the fourth dose and processed for PD (SDMA) or PK (plasma, tumor). For SDMA analysis, see below process: SDMA ELISA. PD and PK data were plotted on the same graph and expressed as mean plus SEM using GraphPad Prism 7.05 software. Statistical significance was computed versus matched control by an ordinary one-way ANOVA at a significance level of 0.05 with Dunnett's multiple comparisons test.

Blood Serum SDMA Assay

On day 28, 24 hours after dosing, whole mouse blood was collected and placed in EDTA-coated collection tubes. Then 120 µL of blood was transferred to a 15-mL conical tube and washed with 10 mL of stain buffer. After centrifugation, the supernatant was aspirated and discarded. The remaining pellet was treated with 2 mL of RBC lysis buffer for 10 minutes, and samples were washed with 10 mL of cold PBS. After centrifugation, the supernatant was aspirated and discarded. Samples were then resuspended in 120 µL of cold PBS; 100 µL of each sample were plated and resuspended in live/dead stain for 30 minutes. After centrifugation, samples were resuspended in an FC block for 15 minutes. After centrifugation, cell surface staining was performed with CD 45.2 antibody. Upon completion of surface staining, samples were then fixed and permeabilized for intracellular staining by SDMA antibody and AF647 fluorochrome. Analysis was performed on a Symphony B flow cytometer. All analyses were performed with FlowJo software v10.9.0. Geometric Mean was calculated as a means of identifying the mean fluorescence intensity of each sample. The average of the group's mean fluorescence intensity was then calculated to assess SDMA inhibition versus the control group.

Cell Line–Derived Xenograft Studies

DOHH-2 (1.0E+07) or BxPC-3 (5.0E+06 with Matrigel) cells were injected subcutaneously in the right flank of female CB17 SCID mice (n = 10/group). HCT116 MTAP WT or HCT116 MTAP-deleted

(2.0E+06 with Matrigel), LU99 (5.0E+06 with Matrigel), or H838 (1.0E+06 with Matrigel) cells were injected subcutaneously in the right flank of female athymic nude mice (n = 10/group). Treatment began when tumors were approximately 169 mm³ (HCT116 MTAP WT), approximately 193 mm³ (HCT116 MTAP-deleted), approximately 115 mm³ (DOHH-2), approximately 122 mm³ (BxPC-3), approximately 166 mm³ (LU99), or 144 mm³ (H838). In the dose-response studies, mice received oral doses of either vehicle (QD) or AMG 193 (3, 10, 30, and 100 mg/kg QD for HCT116 MTAP WT and HCT116 MTAP-deleted; 10, 20, and 30 mg/kg QD for DOHH-2; 10, 30, and 100 mg/kg QD for BxPC-3; 10, 25, and 100 mg/kg QD for LU99 and H838).

PDX HuTrial

Tumor PDXs were selected based on MTAP-deleted status. BB13331 brain, PA13024 pancreatic, PA13004 pancreatic, ME11995 melanoma, PA5379 pancreatic, ME12221 melanoma, LU11554 NS-CLC, ME12091 melanoma, ME12134 melanoma, LU11606 NSCLC, GL11310 gallbladder, OV5287 ovarian, LU5349 NSCLC, LU11672 NSCLC, PA13039 pancreatic, LU5268 NSCLC, LU5194 NSCLC, ME12081 melanoma, LU11894 NSCLC, MU12659 mixed mullerian, ME12183 melanoma, PA5415 pancreatic, ES10084 esophageal, ES11082 esophageal, PA5364 pancreatic PDX studies were performed by Crown Biosciences. NOD/SCID mice were implanted subcutaneously with 2 × 2 mm tumor chunks. Mice were randomized when tumor volumes were ~100 to 150 mm³ (n = 3/group) and received either vehicle (QD) or AM-9747 (100 mg/kg QD) after randomization.

PDX Studies

Tumor PDXs were selected based on MTAP-deleted status. PA5415 pancreatic, LU5268 NSCLC, ME12183 melanoma, and ES11082 esophageal PDX studies were performed by Crown Biosciences. NOD/SCID mice were implanted subcutaneously with 2 × 2 mm tumor chunks. Mice were randomized when tumor volumes were approximately 100 to 150 mm³ (n = 10/group) and received either vehicle (QD) or AMG 193 (25, 50, and 100 mg/kg QD) after randomization.

Combination Studies in CDX and PDX Models

H292 NSCLC (1.0E+07 with Matrigel), MIAPACA2 PDAC (5.0E+06 with Matrigel), or LU99 NSCLC (5.0E+06 with Matrigel) cells were injected subcutaneously in the right flank of female athymic nude mice (n = 10/group). Treatment began when tumors were approximately 120 mm³ (H292) or approximately 180 mm³ (MIAPACA2 and LU99). For the LU5268 NSCLC PDX model, NOD/SCID mice were implanted subcutaneously with tumor chunks (2 × 2 mm). Mice were randomized when tumor volumes were approximately 160 mm³.

In combination with chemotherapy studies, mice received either vehicle 1 (0.1% Tween80: 2% HPMC in deionized (DI) water, pH = 2.0, QD) + vehicle 2 (5% ethanol:5% cremophor EL in D5W, QOD × 5 or D5W, QW × 3); AMG 193 (100 mg QD) + vehicle 2 (5% ethanol:5% cremophor EL in D5W, QOD × 5 or D5W, QW × 3); vehicle 1 + paclitaxel (20 mg/kg, QOD × 5) or carboplatin (60 mg/kg, QW × 3); or AMG 193 (100 mg QD) + paclitaxel (20 mg/kg, QOD × 5) or carboplatin (60 mg/kg, QW × 3). In combination with sotorasib studies, mice received either vehicle 1 (0.1% Tween80, 2% HPMC in DI water, pH = 2.0, QD) + vehicle 2 (30% captisol, pH adjusted to 2.2 with MSA, QD); AMG 193 (100 mg QD) + vehicle 2 (30% captisol, pH adjusted to 2.2 with MSA, QD); vehicle 1 (0.1% Tween80:2% HPMC in DI water, pH = 2.0, QD) + sotorasib (10 mg/kg or 100 mg/kg, QD); or AMG 193 (100 mg QD) + sotorasib (10 mg/kg or 100 mg/kg, QD).

Measurement of AMG 193 in Plasma and Tumor Samples

Blank tumors and tumors collected from the PD study were homogenized in DI water at a ratio of 4-mL water per 1 g tumor using Precellys bead–based homogenizer at 5,500 rpm × 20 seconds

for three cycles. AMG 193 was spiked into blank mouse plasma or blank tumor homogenate to generate calibration curve samples. Plasma and tumor homogenate samples from high-dose groups were further diluted with a blank matrix before quenching in order to be quantified within the linear range; 25 μL of plasma or tumor homogenate samples or calibration curve samples were added with 200 μL of quench solvent, which consisted of 10 ng/mL internal standard (IS, Amgen internal compound) in acetonitrile. The mixture was vortexed at 1,300 rpm for 15 minutes and then centrifuged at 4,500 rpm for 15 minutes. The supernatant was transferred to a new plate and subjected to liquid chromatography—selected reaction monitoring mass spectrometry (LC-SRM MS) analysis. Chromatographic separation was performed using a Phenomenex Kinetex C18 column (2.0 × 50 mm; 1.7 μm; column temperature maintained at 40°C) on a Shimadzu Nexera system. Solvent A contained 0.1% formic acid in water; solvent B contained 0.1% formic acid in acetonitrile. The flow-rate was 400 μL/minute, and the gradient was set as follows: 5%B from 0 to 0.5 minutes, ramped up to 95%B from 0.5 to 2.2 minutes, maintained at 95%B from 2.2 to 2.8 minutes, and then ramped down to 5%B at 2.9 minutes for equilibration. Detection and quantitation of AMG 193 were carried out on a QTRAP 6500 mass spectrometer (Sciex) equipped with an electrospray ionization source, operating in positive ionization mode. For SRM MS analysis, the following transitions were monitored: AMG 193 (445.0/186.1) and IS (604.2/268.3). Data were analyzed using the Quantitate module embedded in Analyst 1.7 (Sciex). Peaks were integrated and the peak area ratios of analyte to IS were used for quantitation. Linear regression (1/×2 weighting, r2 > 0.99) was achieved with LLOQ of 0.3 ng/mL and ULOQ of 5,000 ng/mL for both plasma and tumor homogenate samples.

Pharmacodynamics and MOA In Vivo Assay

DOHH-2 cells were implanted into approximately 6-week-old athymic nude female mice. On day 20 after implantation, mice were measured and randomized (N = 5) as described above and received either vehicle (1% Tween 80, 2% HPMC, pH2.0 w/MSA, QD); noncooperative PRMT5i/LLY-283 (30 mg/kg QD) or AM-9747 (100 mg/kg QD) for 7, 11, or 15 days. At each time point, tumors, bone marrow, and peripheral blood were harvested from each group. Tumors were placed in Liberase TL (0.2 mg/mL; Roche) and DNase I (20 μg/mL; Ambion). Tumor cell suspensions were then homogenized using a gentle MACS Dissociator (Miltenyi Biotech) and incubated at 37°C for 15 minutes on a MACSmix Tube Rotator (Miltenyi Biotech). Cells were then treated with 0.02% EDTA (Sigma-Aldrich) and heat-inactivated FBS (Thermo Fisher Scientific) and filtered to remove clumps. After centrifugation, the cell pellets were resuspended in LIVE/DEAD Fixable Blue Dead Cell Stain (Thermo Fisher Scientific) for 30 minutes. Cell surface staining was performed with the indicated antibodies (Supplementary Table S9) before fixation and permeabilization of the cells (Intracellular Fixation & Permeabilization Buffer Set, eBiosciences) for intracellular staining. CountBright Absolute Counting Beads (Thermo Fisher Scientific) were added to each sample before analysis on an LSR II flow cytometer (BD Biosciences). All analyses were performed with FlowJo software v10 (FlowJo). Absolute cell counts were determined by normalizing cell numbers to beads recorded, divided by the volume of the tumor aliquot analyzed and the mass of the tumor.

Left and right mouse femurs were harvested and extraneous muscle and ligaments were removed with scissors and gauze. Epiphysis was removed using forceps and scissors and an 18G needle was pushed through the bottom of a 1.5-mL Eppendorf tube. Femurs were placed in a 1.5-mL Eppendorf tube and spun at 10,000 × g for 15 seconds. Bone marrow was pelleted at the bottom of the Eppendorf tube and resuspended in cold RPMI and filtered through 70 μm Smartstrainer (Miltenyi). After centrifugation, the cell pellets were

resuspended in RBC lyse buffer for 5 minutes. After washing with PBS and centrifugation, the cell pellets were resuspended in cold PBS for flow cytometry as described above.

Whole mouse blood was collected by cardiac punctuation and placed in EDTA-coated collection tubes. Then, 100 μL of blood was transferred to a new EDTA-coated collection tube with 100 μL of PBS. Blood samples were then run on the ADVIA hematology system (Siemens Healthineers) for phenotyping.

Patient cfDNA Testing

Plasma samples were collected and processed according to standard operating procedures in accordance with Clinical Laboratory Improvement Amendments (CLIA)–certified/College of American Pathologists (CAP) guidelines. Briefly, the 10-mL Streck tubes containing whole blood were gently inverted 8 to 10 times, then centrifuged at $1,500 \times g$ for 15 minutes at 4°C. The plasma was extracted from the top of the tube without disturbing the blood cells and transferred into cryovials at a volume of 2 mL each. These cryovials were stored at −20°C before being submitted to the analytic laboratory. Circulating Free DNA (cfDNA) was extracted and analyzed using the targeted comprehensive cfDNA GuardantINFINITY platform and performed in a CLIA-certified, CAP-accredited, and New York State Department of Health-approved laboratory (Guardant Health). The cTF is estimated from methylation signals across targeted regions of the GuardantINFINITY methylation panel, calibrated using training data from more than 5,000 individuals, including cancer-free donors and patients with mixed cancer types.

Quantitation of Patient Serum SDMA

Serum samples were collected and processed according to standard operating procedures. Serum concentrations of SDMA were measured by using a validated liquid chromatography with tandem mass spectrometry method in a CLIA-certified laboratory (Cleveland HeartLab).

SDMA Imaging Assay, ELISA, and IHC

Details are provided in the Supplementary Materials.

Statistics and Reproducibility

For in vitro studies, statistical analysis was performed using Graph-Pad Prism (GraphPad, RRID:SCR_002798). Unless noted, data are presented as the mean and SE. One-way ANOVA, two-way ANOVA, Pearson correlation coefficient, and unpaired t-test were used as appropriate. P-values were considered significant at *, $P < 0.05$; **, $P < 0.01$; ***, $P < 0.001$; and ****, $P < 0.0001$. No statistical methodologies were used to predetermine the sample size. In vivo studies were performed using standard samples sized for tumor PD ($n = 5$ mice/group) and tumor efficacy ($n = 10$ mice/group). Studies conducted at Amgen were unblinded and were performed once. For animal studies, statistical analysis was performed on treatment groups relative to vehicle alone using Linear Mixed Effects 931 Models implemented within the custom-developed application IVEA (v2.01.00.01) using R 4.1.1 (cran.r-project.org 932 and nlme 3.1.153) package with Dunnett's correction applied for multiplicity. Statistical significance was reported as a P-value of ≤0.05, otherwise considered not significant.

Data availability

Access to the full Cancer DepMap Consortium (DMC) datasets requires DMC membership with the Broad Institute. Cancer cell line feature information is from public sources (https://depmap.org/portal), the DMC, and published reports (28, 44). All RNA-seq data were submitted to Gene Expression Omnibus and assigned repository # GSE273376. Qualified researchers may request de-identified data from Amgen clinical studies; complete details are available at http://www.amgen.com/datasharing.

Authors' Disclosures

B. Belmontes, K.K. Slemmons, C. Su, S. Liu, H. Tan, F. Xie, D.A. Aiello, F. Aeffner, M. Vestergaard, S. Cowland, J. Andersson, I. Sarvary, Q. Chen, P. Sharma, P. Lopez, N. Tamayo, L.H. Pettus, J.R. Allen, J. DeVoss, and A. Coxon report employment with and stock ownership in Amgen, Inc. H. Prenen reports personal fees from Roche, AstraZeneca, Pfizer, Merck, Biocartis, and Amgen outside the submitted work. S. Glad, C.-H. Chuang, K. Keyvanjah, and D.M. Townsley report employment with and stock ownership in Amgen, Inc. M.P. Bourbeau reports personal fees from Amgen, Inc., outside the submitted work and a patent for WO2022169948 pending, a patent for WO2022132914 pending, a patent for WO2022115377 pending, and a patent for WO2021163344 pending. P.E. Hughes reports employment with and stock ownership in Amgen, Inc. No disclosures were reported by the other authors.

Authors' Contributions

B. Belmontes: Conceptualization, formal analysis, supervision, validation, investigation, visualization, methodology, writing–original draft, writing–review and editing. **K.K. Slemmons:** Conceptualization, formal analysis, validation, investigation, visualization, methodology, writing–original draft, writing–review and editing. **C. Su:** Conceptualization, formal analysis, validation, investigation, visualization, methodology, writing–review and editing. **S. Liu:** Conceptualization, formal analysis, validation, investigation, visualization, methodology, writing–review and editing. **A.N. Policheni:** Conceptualization, formal analysis, validation, investigation, visualization, methodology, writing–review and editing. **J. Moriguchi:** Conceptualization, formal analysis, validation, investigation, visualization, methodology, writing–review and editing. **H. Tan:** Conceptualization, formal analysis, validation, investigation, visualization, methodology, writing–review and editing. **F. Xie:** Conceptualization, formal analysis, validation, investigation, visualization, methodology, writing–review and editing. **D.A. Aiello:** Conceptualization, formal analysis, validation, investigation, visualization, methodology, writing–review and editing. **Y. Yang:** Conceptualization, validation, investigation, visualization, methodology, writing–review and editing. **R. Lazaro:** Conceptualization, formal analysis, validation, investigation, visualization, methodology, writing–review and editing. **F. Aeffner:** Conceptualization, formal analysis, validation, investigation, visualization, writing–review and editing. **M.G. Rees:** Conceptualization, formal analysis, validation, investigation, visualization, methodology, writing–review and editing. **M.M. Ronan:** Conceptualization, formal analysis, validation, investigation, visualization, methodology, writing–review and editing. **J.A. Roth:** Conceptualization, formal analysis, validation, investigation, visualization, methodology, writing–review and editing. **M. Vestergaard:** Conceptualization, formal analysis, validation, investigation, visualization, methodology, writing–review and editing. **S. Cowland:** Conceptualization, formal analysis, validation, investigation, visualization, methodology, writing–review and editing. **J. Andersson:** Conceptualization, formal analysis, validation, investigation, visualization, methodology, writing–review and editing. **I. Sarvary:** Conceptualization, formal analysis, validation, investigation, visualization, methodology, writing–review and editing. **Q. Chen:** Conceptualization, formal analysis, validation, investigation, visualization, methodology, writing–review and editing. **P. Sharma:** Conceptualization, formal analysis, validation, investigation, visualization, methodology, writing–review and editing. **P. Lopez:** Conceptualization, formal analysis, validation, investigation, visualization, methodology, writing–review and editing.

REFERENCES

1. Bedard PL, Hyman DM, Davids MS, Siu LL. Small molecules, big impact: 20 years of targeted therapy in oncology. Lancet 2020;395: 1078–88.
2. Lucchesi JC. Synthetic lethality and semi-lethality among functionally related mutants of drosophila melanfgaster. Genetics 1968;59: 37–44.
3. Bryant HE, Schultz N, Thomas HD, Parker KM, Flower D, Lopez E, et al. Specific killing of BRCA2-deficient tumours with inhibitors of poly(ADP-ribose) polymerase. Nature 2005;434:913–7.
4. Farmer H, McCabe N, Lord CJ, Tutt AN, Johnson DA, Richardson TB, et al. Targeting the DNA repair defect in BRCA mutant cells as a therapeutic strategy. Nature 2005;434:917–21.
5. Lord CJ, Ashworth A. PARP inhibitors: synthetic lethality in the clinic. Science 2017;355:1152–8.
6. Huang A, Garraway LA, Ashworth A, Weber B. Synthetic lethality as an engine for cancer drug target discovery. Nat Rev Drug Discov 2020;19:23–38.
7. Mavrakis KJ, McDonald ER III, Schlabach MR, Billy E, Hoffman GR, deWeck A, et al. Disordered methionine metabolism in MTAP/CDKN2A-deleted cancers leads to dependence on PRMT5. Science 2016;351:1208–13.
8. Kryukov GV, Wilson FH, Ruth JR, Paulk J, Tsherniak A, Marlow SE, et al. MTAP deletion confers enhanced dependency on the PRMT5 arginine methyltransferase in cancer cells. Science 2016;351: 1214–8.
9. Marjon K, Cameron MJ, Quang P, Clasquin MF, Mandley E, Kunii K, et al. MTAP deletions in cancer create vulnerability to targeting of the MAT2A/PRMT5/RIOK1 axis. Cell Rep 2016;15:574–87.
10. Engstrom LD, Aranda R, Waters L, Moya K, Bowcut V, Vegar L, et al. MRTX1719 is an MTA-cooperative PRMT5 inhibitor that exhibits synthetic lethality in preclinical models and patients with MTAP-deleted cancer. Cancer Discov 2023;13:2412–31.
11. Fong JY, Pignata L, Goy P-A, Kawabata KC, Lee SC-W, Koh CM, et al. Therapeutic targeting of RNA splicing catalysis through inhibition of protein arginine methylation. Cancer Cell 2019;36:194–209.e9.
12. Wu Q, Schapira M, Arrowsmith CH, Barsyte-Lovejoy D. Protein arginine methylation: from enigmatic functions to therapeutic targeting. Nat Rev Drug Discov 2021;20:509–30.
13. Liang Z, Wen C, Jiang H, Ma S, Liu X. Protein arginine methyltransferase 5 functions via interacting proteins. Front Cell Dev Biol 2021;9:725301.
14. Rodon J, Rodriguez E, Maitland ML, Tsai FY, Socinski MA, Berlin JD, et al. A phase I study to evaluate the safety, pharmacokinetics, and pharmacodynamics of PF-06939999 (PRMT5 inhibitor) in patients with selected advanced or metastatic tumors with high incidence of splicing factor gene mutations. ESMO Open 2024;9:102961.
15. Haque T, Cadenas FL, Xicoy B, Alfonso-Pierola A, Platzbecker U, Avivi I, et al. Phase 1 study of JNJ-64619178, a protein arginine methyltransferase 5 inhibitor, in patients with lower-risk myelodysplastic syndromes. Leuk Res 2023;134:107390.
16. Feustel K, Falchook GS. Protein arginine methyltransferase 5 (PRMT5) inhibitors in oncology clinical trials: a review. J Immunother Precis Oncol 2022;5:58–67.
17. Vieito M, Moreno V, Spreafico A, Brana I, Wang JS, Preis M, et al. Phase 1 study of JNJ-64619178, a protein arginine methyltransferase 5 inhibitor, in advanced solid tumors. Clin Cancer Res 2023;29: 3592–602.
18. Kontijevskis A. Mapping of drug-like chemical universe with reduced complexity molecular frameworks. J Chem Inf Model 2017;57: 680–99.
19. Ahn S, Kahsai AW, Pani B, Wang Q-T, Zhao S, Wall AL, et al. Allosteric "beta-blocker" isolated from a DNA-encoded small molecule library. Proc Natl Acad Sci U S A 2017;114:1708–13.
20. Belmontes B, Policheni A, Liu S, Slemmons K, Moriguchi J, Ma H, et al. Abstract 1807: the discovery and preclinical characterization of the MTA cooperative PRMT5 inhibitor AM-9747. Cancer Res 2022;82:1807.
21. Smith CR, Aranda R, Bobinski TP, Briere DM, Burns AC, Christensen JG, et al. Fragment-based discovery of MRTX1719, a synthetic lethal inhibitor of the PRMT5·MTA complex for the treatment of MTAP-deleted cancers. J Med Chem 2022;65:1749–66.
22. Quinn JG, Pitts KE, Steffek M, Mulvihill MM. Determination of affinity and residence time of potent drug-target complexes by label-free biosensing. J Med Chem 2018;61:5154–61.
23. Bonday ZQ, Cortez GS, Grogan MJ, Antonysamy S, Weichert K, Bocchinfuso WP, et al. LLY-283, a potent and selective inhibitor of arginine methyltransferase 5, PRMT5, with antitumor activity. ACS Med Chem Lett 2018;9:612–7.

24. Kalev P, Hyer ML, Gross S, Konteatis Z, Chen CC, Fletcher M, et al. MAT2A inhibition blocks the growth of MTAP-deleted cancer cells by reducing PRMT5-dependent mRNA splicing and inducing DNA damage. Cancer Cell 2021;39:209–24.e11.

25. Braun CJ, Stanciu M, Boutz PL, Patterson JC, Calligaris D, Higuchi F, et al. Coordinated splicing of regulatory detained introns within oncogenic transcripts creates an exploitable vulnerability in malignant glioma. Cancer Cell 2017;32:411–26.e11.

26. Yu C, Mannan AM, Yvone GM, Ross KN, Zhang YL, Marton MA, et al. High-throughput identification of genotype-specific cancer vulnerabilities in mixtures of barcoded tumor cell lines. Nat Biotechnol 2016;34:419–23.

27. Corsello SM, Nagari RT, Spangler RD, Rossen J, Kocak M, Bryan JG, et al. Discovering the anti-cancer potential of non-oncology drugs by systematic viability profiling. Nat Cancer 2020;1:235–48.

28. Ghandi M, Huang FW, Jané-Valbuena J, Kryukov GV, Lo CC, McDonald ER III, et al. Next-generation characterization of the cancer cell line encyclopedia. Nature 2019;569:503–8.

29. Zhang L, Yang J, Cai J, Song X, Deng J, Huang X, et al. A subset of gastric cancers with EGFR amplification and overexpression respond to cetuximab therapy. Sci Rep 2013;3:2992.

30. Chen D, Huang X, Cai J, Guo S, Qian W, Wery JP, et al. A set of defined oncogenic mutation alleles seems to better predict the response to cetuximab in CRC patient-derived xenograft than KRAS 12/13 mutations. Oncotarget 2015;6:40815–21.

31. Gao H, Korn JM, Ferretti S, Monahan JE, Wang Y, Singh M, et al. High-throughput screening using patient-derived tumor xenografts to predict clinical trial drug response. Nat Med 2015;21:1318–25.

32. Ashok Kumar P, Graziano SL, Danziger N, Pavlick D, Severson EA, Ramkissoon SH, et al. Genomic landscape of non-small-cell lung cancer with methylthioadenosine phosphorylase (MTAP) deficiency. Cancer Med 2023;12:1157–66.

33. Rodon J, Yamamoto N, Doi T, Ghiringhelli F, Goebeler M, Fujuwara Y, et al. Abstract PR006: initial results from first-in-human study of AMG 193, an MTA-cooperative PRMT5 inhibitor, in biomarker-selected solid tumors. Mol Cancer Ther 2023;22(Suppl 12):PR006.

34. Liu F, Cheng G, Hamard P-J, Greenblatt S, Wang L, Man N, et al. Arginine methyltransferase PRMT5 is essential for sustaining normal adult hematopoiesis. J Clin Invest 2015;125:3532–44.

35. Briggs KJ, Tsai A, Zhang M, Tonini MR, Haines B, Huang A, et al. Abstract 4970: TNG462 is a potential best-in-class MTA-cooperative PRMT5 inhibitor for the treatment of MTAP-deleted solid tumors. Cancer Res 2023;83(Suppl 7):4970.

36. Lynch JT, Moore S, Barrantes IDB, Bradshaw L, Chambers C, Hong T, et al. Abstract 6272: AZ-PRMT5i-1: a potent MTAP-selective PRMT5 inhibitor with pharmacodynamic and monotherapy anti-tumor activity in MTAP-deleted tumours. Cancer Res 2023;83(Suppl 7):6272.

37. Aldea M, Andre F, Marabelle A, Dogan S, Barlesi F, Soria JC. Overcoming resistance to tumor-targeted and immune-targeted therapies. Cancer Discov 2021;11:874–99.

38. Chou T-C. Drug combination studies and their synergy quantification using the Chou-Talalay method. Cancer Res 2010;70:440–6.

39. Kahles A, Ong CS, Zhong Y, Rätsch G. SplAdder: identification, quantification and testing of alternative splicing events from RNA-Seq data. Bioinformatics 2016;32:1840–7.

40. Yu G, Wang L-G, Han Y, He Q-Y. clusterProfiler: an R package for comparing biological themes among gene clusters. OMICS 2012;16:284–7.

41. Antonysamy S, Bonday Z, Campbell RM, Doyle B, Druzina Z, Gheyi T, et al. Crystal structure of the human PRMT5:MEP50 complex. Proc Natl Acad Sci U S A 2012;109:17960–5.

42. Emsley P, Cowtan K. Coot: model-building tools for molecular graphics. Acta Crystallogr D Biol Crystallogr 2004;60:2126–32.

43. Adams PD, Afonine PV, Bunkóczi G, Chen VB, Echols N, Headd JJ, et al. The Phenix software for automated determination of macromolecular structures. Methods 2011;55:94–106.

44. Tsherniak A, Vazquez F, Montgomery PG, Weir BA, Kryukov G, Cowley GS, et al. Defining a cancer dependency map. Cell 2017;170:564–76.e16.